Article

Supercritical density fluctuations and structural heterogeneity in supercooled water-glycerol microdroplets

Sharon Berkowicz[1,7], Iason Andronis [1,7], Anita Girelli [1], Mariia Filianina [1], Maddalena Bin [1], Kyeongmin Nam [2], Myeongsik Shin [2], Markus Kowalewski [1], Tetsuo Katayama [3,4], Nicolas Giovambattista [5,6], Kyung Hwan Kim [2] & Fivos Perakis [1] ✉

Recent experiments and theoretical studies strongly indicate that water exhibits a liquid-liquid phase transition (LLPT) in the supercooled domain. An open question is how the LLPT of water can affect the properties of aqueous solutions. Here, we study the structural and thermodynamic properties of supercooled glycerol-water microdroplets at dilute conditions (χ_g = 3.2% glycerol mole fraction). The combination of rapid evaporative cooling with femtosecond X-ray scattering allows us to outrun crystallization and gain access to the deeply supercooled regime down to T = 229.3 K. We find that the density fluctuations of the glycerol-water solution or, equivalently, its isothermal compressibility, κ_T, increases upon cooling. This is confirmed by molecular dynamics simulations, which indicate that the presence of glycerol shifts the temperature of maximum κ_T from T = 230 K in pure water down to T = 223 K in the solution. Our findings elucidate the interplay between the complex behavior of water, including its LLPT, and the properties of aqueous solutions at low temperatures, which can have practical consequences in cryogenic biological applications and cryopreservation techniques.

The thermodynamic behavior of water is complex[1-4]. For example, in the liquid state and at P = 1 bar, water exhibits anomalous maxima in density $\rho(T)$ (at T = 277 K)[5], isobaric heat capacity $C_P(T)$ (at T = 229 K)[6], and isothermal compressibility $\kappa_T(T)$ (at T = 230 K)[7]. A natural explanation of the anomalous behavior of liquid and glassy water is given by the liquid–liquid phase transition (LLPT) hypothesis[8] which has received overwhelming support in recent years from experiments[6,7,9-12] and theoretical investigations[13-15]. In the LLPT scenario, liquid water exists in two liquid states at very low temperatures (at approximately T < 220 K), low-density liquid (LDL) at low pressures, and high-density liquid (LDL) at elevated pressures.

In the P–T plane, LDL and HDL are separated by a (liquid–liquid) first-order phase transition line at very low temperatures that ends at a liquid–liquid critical point (LLCP) located at approximately P_c = 50–100 MPa and T_c = 200–220 K[16-18]. According to this hypothesis, liquid water at $T > T_c$ and ambient pressure is a supercritical mixture of HDL/LDL fluctuating domains[3,8,18,19]. In particular, the presence of the LLCP in the P–T phase diagram of water implies that the liquid must exhibit lines of maxima (in the P–T plane) in $\kappa_T(T)$ and $C_P(T)$ at constant pressure ($P < P_c$). These lines of maxima in $\kappa_T(T)$ and $C_P(T)$ converge onto a single line in the P–T plane as $P \to P_c$, defining the so-called Widom line—specifically, the Widom line

[1]Department of Physics, AlbaNova University Center, Stockholm University, SE-10691 Stockholm, Sweden. [2]Department of Chemistry, Pohang University of Science and Technology (POSTECH), Pohang 37673, Republic of Korea. [3]Japan Synchrotron Radiation Research Institute, Kouto 1-1-1, Sayo Hyogo 679-5198, Japan. [4]RIKEN SPring-8 Center, Kouto 1-1-1, Sayo Hyogo 679-5148, Japan. [5]Department of Physics, Brooklyn College of the City University of New York, Brooklyn NY 11210, USA. [6]The Graduate Center of the City University of New York, New York NY 10016, USA. [7]These authors contributed equally: Sharon Berkowicz, Iason Andronis. ✉e-mail: f.perakis@fysik.su.se

corresponds to the states in the $P-T$ plane at which the correlation length reaches a maximum value[20]. The location of the Widom line at ambient pressure has been observed experimentally, indicating that liquid water exhibits maxima in the correlation length at $T \approx 230$ K[7]. In particular, a maximum in $\kappa_T(T)$ and $C_P(T)$ have also been identified at $T \approx 230$ K at ambient pressure[6,7], implying that the LLCP in water must be located at slightly elevated pressures[18]. While the hypothesized LLCP in liquid water has been found in numerous molecular dynamics (MD) simulations using different realistic water models[15,21–25], it has so far eluded direct experimental verification.

The LDL-HDL fluctuations in liquid water at ambient pressure and low temperatures may have significant implications for the thermodynamic, structural, and dynamic properties of aqueous solutions. For example, at dilute concentrations, they should induce maxima in thermodynamic response functions, such as $C_P(T)$ and $\kappa_T(T)$, which are associated with fluctuations in enthalpy and density, respectively. LDL-HDL fluctuations may also affect the solvation of biomolecules both at ambient and supercooled conditions. The behavior of supercooled liquid and glassy aqueous solutions has wide importance in scientific and engineering applications, such as in cryopreservation techniques and the study of biological matter at low and cryogenic temperatures. Cryoprotectants are often utilized to minimize freeze damage, by interrupting the hydrogen-bond network of water and thereby preventing ice nuclei from forming and growing[26,27]. Interestingly, it has been suggested that the addition of solutes to water can affect the hydrogen-bond structure in a manner that resembles increasing pressure, i.e. by suppressing the tetrahedral hydrogen-bonded water structures associated with LDL[28–30].

The following natural questions arise from our discussion above: do the LLPT and/or the HDL/LDL fluctuations observed in pure water also exist in aqueous mixtures? If so, at what concentrations do the LLPT and LDL/HDL fluctuations develop in the solution? What role do they play in the behavior/properties of the solution? We note that MD simulations indicate that an LLCP may exist in ionic aqueous solutions, although the location of the critical point in the phase diagram can be shifted relative to pure bulk water due to the presence of the solutes and how these interact with water[30–34]. This observation is also consistent with experiments of hyperquenched aqueous LiCl solutions, where a polyamorphic transition from high-density to low-density glass was observed[35–38]. MD simulations and experiments in glassy water also suggest that an LLPT may occur in dilute aqueous solutions containing alcohols and/or biomolecules[39].

Glycerol-water mixtures of different concentrations have become prototypical systems to study whether the LLPT and/or HDL/LDL fluctuations can manifest in organic aqueous solutions[28,29,40–46]. Experiments show that, upon isobaric cooling, solutions with intermediate glycerol concentrations ($\chi_g = 13-19\%$ glycerol mole fraction) develop noticeable changes in the liquid structure. These changes were originally believed to stem from a low-temperature LLPT in the solution, related to the HDL/LDL fluctuations in pure water[28,29,45]. However, further experiments and simulations attributed the low-temperature solution behavior at intermediate glycerol concentrations primarily to the formation of ice crystallites and freeze-concentration of the remaining solution[41–45,47]. Nonetheless, at least for very dilute glycerol-water solutions, it is expected that the LLCP location in the $P-T$ plane, (P_c, T_c), shifts continuously with the addition of glycerol. Indeed, MD simulations and experiments in glassy glycerol-water solutions suggest that the LLCP shifts towards lower temperatures and/or higher pressures in the presence of glycerol, e.g., ($T_c = 150$ K, $P_c = 30-50$ MPa) for $\chi_g = 12-15\%$ glycerol mole fraction[40,42,43]. We note that experiments confirming the existence of an LLCP in supercooled liquid glycerol-water solutions have so far been missing due to the fast ice nucleation in the samples which is difficult to avoid experimentally[41–45,47,48].

In this work, we probe experimentally the liquid structure and thermodynamic properties of deeply supercooled microdroplets of glycerol-water solutions in the dilute regime ($\chi_g = 3.2\%$ glycerol mole fraction) down to $T = 229.3$ K, which is not accessible by conventional methods. Our goal is to address the following questions: how does the LLPT of water affect the properties of dilute glycerol-water mixtures? How does the presence of glycerol affect the local water network structure and the LDL-HDL fluctuations? In particular, how does the addition of glycerol shift the reported maximum in the compressibility of pure water? Our approach utilizes the rapid evaporative cooling technique[7,9] combined with femtosecond X-ray scattering at SACLA X-ray free-electron laser (XFEL) (see Fig. 1). The use of a large-area detector enables us to measure simultaneously the wide-and small-angle x-ray scattering domains (WAXS and SAXS) of the structure factor $S(q)$. In particular, from the SAXS measurements, we extract the isothermal compressibility and correlation length of the associated density fluctuations. In addition, we complement the experimental results with molecular dynamics (MD) simulations. The MD simulations allow us to study the properties of the solution, including $S(q)$, κ_T, and the local molecular structure, down to $T = 190$ K ($\chi_g = 3.2\%$ glycerol mole fraction).
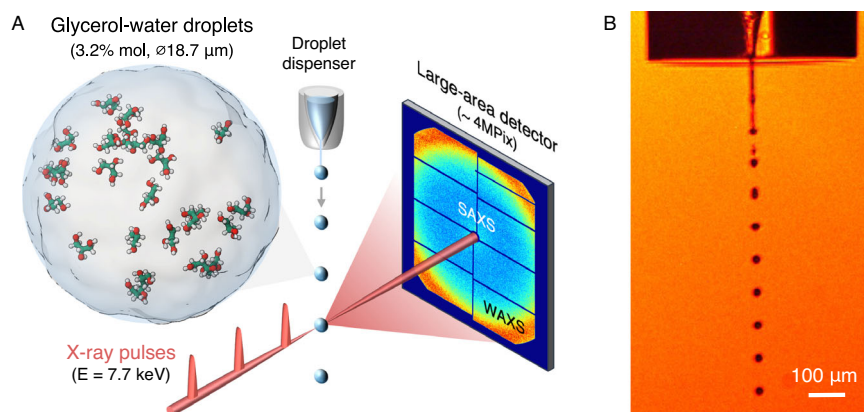

Fig. 1 | The experimental setup combining rapid evaporative cooling of glycerol-water microdroplets with femtosecond X-ray scattering. A A schematic overview of the experiment where glycerol-water solution ($\chi_g = 3.2\%$ glycerol mole fraction) is supercooled by rapid evaporation in vacuum and probed by femtosecond X-ray pulses at SACLA X-ray free-electron laser (XFEL). The small- and wide-angle X-ray scattering (SAXS, WAXS) are measured simultaneously by using a large-area detector. **B** Microscope image of the glycerol-water droplets (18.7 μm in diameter) shown close to the liquid jet nozzle, recorded by stroboscopic illumination.
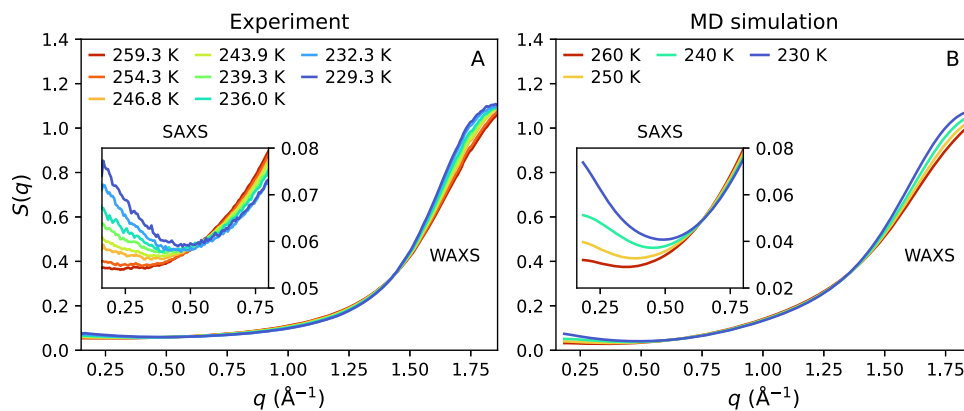
Fig. 2 | The small- and wide-angle X-ray scattering (SAXS, WAXS) structure factor $S(q)$ of glycerol-water solutions (χ_g = 3.2% glycerol mole fraction) at different temperatures. Comparison of $S(q)$ obtained by (**A**) femtosecond X-ray scattering experiments on microdroplets and (**B**) molecular dynamics (MD) simulations. The insets show magnifications of the SAXS region (note the different scale on the y-axis of the insets in (**A**) and (**B**)).

Results

X-ray structure factor

Figure 2A shows the experimental structure factor of supercooled droplets (18.7 μm in diameter) containing dilute glycerol-water solutions (χ_g = 3.2% glycerol mole fraction) at different temperatures probed by femtosecond X-ray scattering at SACLA XFEL. A large-area detector is used that provides a broad momentum transfer q-range spanning from SAXS ($q_{min} \approx 0.15$ Å^{-1}) to the first diffraction peak in WAXS ($q_{max} \approx 1.89$ Å^{-1}). We also measure the structure factor of bulk glycerol-water solutions (χ_g = 3.2% glycerol mole fraction) by table-top X-ray diffraction (XRD) at temperatures T = 295–250 K. This allows us to measure the $S(q)$ over a larger q-range, up to $q \approx 6$ Å^{-1}; see Supplementary Information for details on the calculations of $S(q)$, reproducibility, and control of experimental conditions. Upon cooling, the first peak of $S(q)$ increases in magnitude and, in particular, it shifts continuously towards lower values of q. This observation is consistent with the behavior of the $S(q)$ in pure water, reflecting the increasing tetrahedral coordination of the water molecules upon cooling[7]. The SAXS region is emphasized in the inset of Fig. 2A, where a strong enhancement of the structure factor is observed with decreasing temperature. This SAXS enhancement is also consistent with previous experiments in supercooled pure water, which is attributed to the increase of density fluctuations and hence, to the increase of isothermal compressibility, upon cooling[7].

Interestingly, there is an isosbestic point in the $S(q)$ shown in Fig. 2A located at $q \approx 0.5$ Å^{-1}. While it is not evident whether there is an underlying physical/chemical reason for the existence of this isosbestic point in the $S(q)$, such an isosbestic point defines a T-independent wavevector q that can be used as a useful for future SAXS studies. The isosbestic point in $S(q)$ is a consequence of the increase in $S(0)$ upon cooling, which is due to the increase in thermal compressibility as the temperature of the solution is lowered. Since the value of $S(q_1)$ is practically T-independent, the increase of $S(0)$ upon cooling leads to an isosbestic point that barely shifts with decreasing temperature. An isosbestic point is also found in the $S(q)$ of pure water, located at $q \approx 0.4$ Å^{-17}. MD simulations using TIP4P/2005 indicate an isosbestic point at $q \approx 0.25$ Å^{-1} at P = 1 bar, which shifts to $q \approx 0.4$ Å^{-1} upon increasing pressure at P = 1 kbar[49]. Accordingly, adding glycerol shifts the isosbestic point of the $S(q)$ slightly, towards higher q-values, at $q \approx 0.5$ Å^{-1}, which is consistent with the overall shift in the $S(q)$ of water, towards lower values of q, with the addition of glycerol. A similar shift of the isosbestic point of the $S(q)$ has been measured in the SAXS of NaCl-water solutions[50,51], resembling the trend found in computer simulations of pure water with increasing pressure[22].

Figure 2B shows the $S(q)$ of the glycerol-water solutions (χ_g = 3.2% glycerol mole fraction) calculated from MD simulations at temperatures T = 230–260 K (see the Methods for details on the computer simulations). Qualitatively, the experimental and simulated structure factors show remarkable resemblance. In agreement with the experiments (Fig. 2A), the $S(q)$ obtained from the MD simulations exhibits a shift in the diffraction peak towards lower q-values and a pronounced enhancement of the SAXS intensity upon supercooling. On comparing the SAXS structure factors from experiments and MD simulations (see insets, Fig. 2), we note two main differences. Firstly, there is a slight shift in the q-position of the experimental and simulated isosbestic points of $S(q)$ (in the SAXS range). This is in agreement with previous observations in the $S(q)$ of pure water obtained from experiments/MD simulations[22]. Secondly, there is a small difference in the absolute intensity of the SAXS curves at small q. For example the minimum of $S(q)$ in Fig. 2A increases from $S(q) \approx 0.055$ to $S(q) \approx 0.060$ as the temperature decreases from $T \approx 260$ K to $T \approx 230$ K. Instead, in Fig. 2B, the minimum of $S(q)$ increases from $S(q) \approx 0.030$ to $S(q) \approx 0.040$ (for the same T-interval). This discrepancy is likely due to the difference in the $S(0)$ between experiments and MD simulations observed also for pure water[49], related to the fact that TIP4P/2005 underestimates the compressibility, (see Supplementary Note 5 for a direct comparison and detailed discussion). A small difference in the vertical offset and scaling of the SAXS curves can also result from the dilute-limit approximation used for the calculation of the $S(q)$ from the MD simulations (see Supplementary Note 1) or from experimental uncertainties arising from the background subtraction (see Supplementary Note 1.1).

Taking into account the difference in melting temperature of real water and TIP4P/2005 ($T_m \approx 250$ K), and thus comparing supercooled degrees instead of the absolute temperature is not sufficient by itself to account for the observed discrepancy (see Supplementary Supplementary Fig. 10). It has been shown that comparing the experimental data of pure water with MD simulations at elevated pressures yields a more accurate comparison of the SAXS regime and the corresponding compressibility[49]. This effect can be attributed to the fact that the location of the LLCP of the TIP4P/2005 model (see refs. 15,22–25,52) is shifted in pressure–temperature with respect to the LLCP estimation in real water[18].

Wide-angle X-ray scattering (WAXS)

The structure factor first-peak position of the glycerol-water solution, $q_1(T)$, is shown in Fig. 3A for T = 229.3-295 K. Included in Fig. 3A are the values of $q_1(T)$ extracted from (i) the WAXS measurements of microdroplets at SACLA XFEL (T = 229.3–250 K; open black circles)
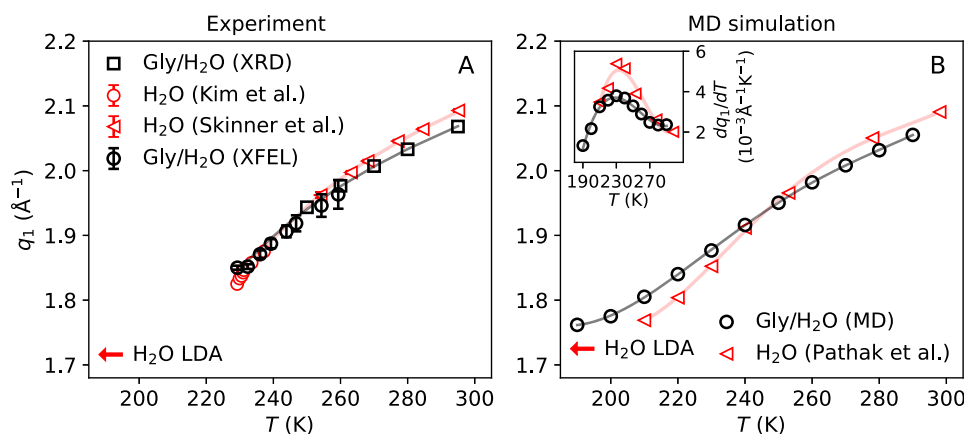
Fig. 3 | Temperature-dependence of the structure factor first-peak position, $q_{1(T)}$, obtained from wide-angle X-ray scattering (WAXS) and MD simulations. **A** Experimental data for the glycerol-water solutions (χ_g = 3.2% glycerol mole fraction) obtained from WAXS measurements using table-top X-ray diffraction (XRD) at moderately supercooled temperatures ($T \geq 250$–295 K, open black squares), and by femtosecond X-ray scattering of evaporatively cooled microdroplets (T = 229.3–250 K, open black circles). For comparison, we include the experimental $q_1(T)$ of pure liquid water (open red circles and triangles) from refs. 7,53. **B** $q_1(T)$ obtained from MD simulations of glycerol-water solutions (χ_g = 3.2% glycerol mole fraction, open

black circles) and pure liquid water from ref. 49 (open red triangles). Solid lines are smoothing spline fits. The inset in (**B**) shows the temperature-derivative dq_1/dT for the glycerol-water solution (open black circles) and pure water (open red triangles). The maximum in dq_1/dT occurs at T = 228 K for the glycerol-water solution and at T = 233 K for pure water, respectively. In both figures, error bars smaller than the size of the corresponding data points and the red arrows are used to indicate the q_1 of low-density amorphous (LDA) ice, according to experiments[84] at T = 80 K, and simulations[85] at T = 80 K. Error bars indicate the standard error obtained from the gaussian fit to the first $S(q)$ peak.

and (ii) the bulk solution using table-top XRD (T = 250-295 K; open black squares). With conventional cooling methods, i.e., with cooling rates of ~1 K/s, the lowest temperature accessible to the glycerol-water solution before crystallization intervenes is $T \approx 250$ K (3.2% glycerol mole fraction). The use of evaporative rapid cooling of microdroplets allows us to extend the experimental data down to T = 229.3 K (see Supplementary Note 3 for details on the temperature estimation). Within the measured temperature range, T = 229.3–295 K, $q_1(T)$ decreases continuously upon cooling. In addition, the experimental data indicates that the corresponding rate of change, $dq_1(T)/dT$, increases upon cooling. This trend is consistent with the temperature dependence of $q_1(T)$ measured in pure water (open red triangles and circles from refs. 7,53). In the case of pure water, it has been shown that the decrease of $q_1(T)$ upon cooling is correlated with an increase in the tetrahedral order of the water molecules[7]. Interestingly, Fig. 3A shows that at high temperatures, approximately $T > 250$ K, the addition of glycerol reduces the values of q_1 at a given temperature, while at $230 < T < 250$ K, the $q_1(T)$ of pure water and the glycerol-water solution nearly overlap. This suggests that, at least for $T > 250$ K, glycerol promotes a comparatively more open tetrahedral arrangement of solvent molecules, relative to bulk water. The ability of glycerol to form multiple hydrogen bonds can play a key role, enabling glycerol to incorporate itself within the hydrogen-bond network of water.

Figure 3B shows the $q_1(T)$ for the glycerol-water solution calculated from our MD simulations (open black circles) as well as the corresponding results obtained for bulk TIP4P/2005 water reported in ref. 49. Overall, the results from the MD simulations shown in Fig. 3B are in semi-quantitative agreement with the experimental data (Fig. 3A); see also Supplementary Fig. 6A. While the experimental data is limited to $T \geq 229.3$ K due to rapid crystallization, the lack of crystallization in the MD simulations allows us to explore the behavior of $q_1(T)$ at lower temperatures. As shown in Fig. 3B, two temperature regimes can be identified: a high-temperature regime ($T > 240$ K) where the $q_1(T)$ of the glycerol-water solution is lower than the $q_1(T)$ of pure water, and a low-temperature regime ($T < 240$ K) where the $q_1(T)$ of the glycerol-water is higher than that of pure water. It follows that at low temperatures, the addition of glycerol shifts the first peak of $S(q)$ towards larger values, relative to the pure water case, suggesting that

at $T < 240$ K glycerol may partially suppress the local tetrahedral structure of water.

We conclude this section by noticing that the MD simulation of glycerol-water solutions show an inflection point in $q_1(T)$ at around T = 231 K, yielding a maximum in the temperature-derivative dq_1/dT (see the inset of Fig. 3B). This temperature is practically identical to the Widom line temperature in pure water at ambient pressure reported in ref. 21. Importantly, in the case of pure water, a maximum in the experimental dq_1/dT has also been reported at $T \approx 230$ K which coincides with the experimental Widom line temperature of pure water at ambient pressure[7] (based on the maxima in correlation length).

Small-angle X-ray scattering (SAXS)

Next, we focus on the features of $S(q)$ at $q < 0.5\,\text{Å}^{-1}$. An enhancement of the $S(q)$ in the SAXS region upon supercooling (Fig. 2) is associated with the presence of density fluctuations[7,50,51]. Indeed, the isothermal compressibility κ_T, which is the thermodynamic response function that quantifies the density fluctuations in the system, is given by[54]

$$\kappa_T = \frac{S(0)}{nk_BT}. \tag{1}$$

where n is the average molecular number density in the solution estimated from the corresponding total density and average molecular mass (see Supplementary Note 2); k_B is the Boltzmann constant. The correlation length associated with the density fluctuations, $\xi(T)$, can also be extracted from the SAXS measurements (see Methods and Supplementary Fig. 5).

Figure 4A shows the experimental $\kappa_T(T)$ of glycerol-water solution obtained using Eq. (1) (black open circles). Also included is the $\kappa_T(T)$ for bulk water reported in the experiments of ref. 7 (empty red triangles). In both cases, $\kappa_T(T)$ increases rapidly upon cooling. A similar trend is seen in the correlation length $\xi(T)$ (see Supplementary Fig. 4B). Compared to pure water (solid red line, Fig. 4A)[55], the isothermal compressibility for the glycerol-water solution is significantly lower over the entire experimental temperature range T = 229.3–295 K. This indicates that even though the glycerol-water system exhibits anomalous density fluctuations that increase upon cooling, such fluctuations are less pronounced than in pure water. It follows that the
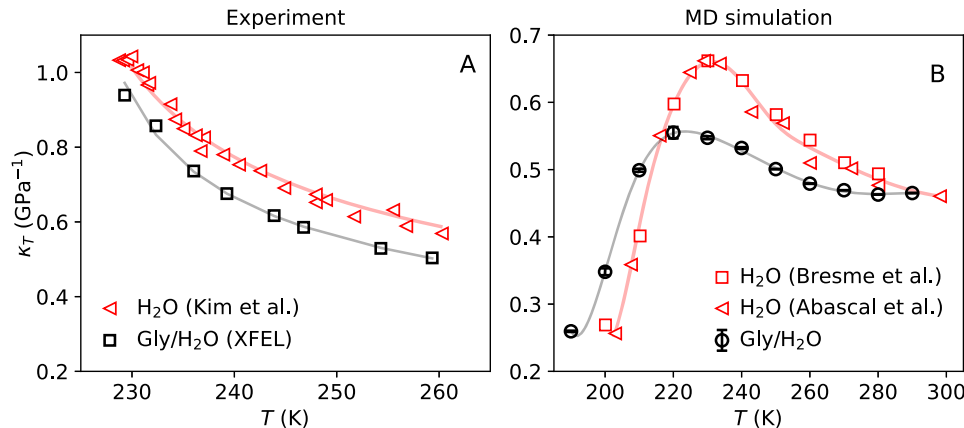
Fig. 4 | Temperature-dependence of the isothermal compressibility κ_T.
A Isothermal compressibility, κ_T, of glycerol-water solutions (χ_g = 3.2% glycerol mole fraction, black open circles) calculated from the structure factor obtained using the femtosecond X-ray scattering (SAXS). Also included is the κ_T of pure water from the SAXS experiments reported in ref. 7 (open red triangles). Solid lines are power-law fits to the data using Eq. (2)[55] (see also Table 1). **B** The $\kappa_T(T)$ of the glycerol-water solution (χ_g = 3.2% glycerol mole fraction, black open circles) and pure TIP4P/2005 water obtained from MD simulations (open red triangles[21] and squares[86]). A maximum in $\kappa_T(T)$ is found in the MD simulations of both pure TIP4P/2005 water (T = 234 K) and glycerol-water solutions (T = 223 ± 1 K). The solid lines are spline interpolations to the data. Note the difference in the scale of the x and y axis between the panels. Error bars indicate the standard error.

presence of glycerol partially disrupts the collective density fluctuations of water by (i) direct interactions with the water molecules, and/or (ii) by effectively inducing confinement effects which may suppress the size of the high/low-density transient domains.

We fit the experimental values of $\kappa_T(T)$ and $\xi(T)$ to power-law relations[54,55], specifically,

$$\kappa_T(T) = \kappa_{T,0}\,\epsilon^{-\gamma} \quad \text{and} \quad \xi(T) = \xi_0\,\epsilon^{-\nu}, \qquad (2)$$

where $\epsilon = (T - T_s)/T_s$ and T_s is the temperature at which each property diverges. The ξ_0 and $\kappa_{T,0}$ are constants; ν and γ are the associated power law exponents. The fit to the experimental values of $\kappa_T(T)$, using Eq. (2), is included in Fig. 4A (black solid line). The corresponding exponent and characteristic temperature are γ = 0.36 ± 0.02 and $T_{s,\kappa}$ = 224 ± 1 K. Similar results hold for the correlation length (see Supplementary Fig. 4B), with corresponding exponent and temperatures being ν = 0.26 ± 0.1 and $T_{s,\xi}$ = 221 ± 7 K. The power-law fitting parameters are given in Table 1 and are close to the corresponding values reported from experiments in pure water[55]. If the power law behavior in $\kappa_T(T)$ and $\xi(T)$ was due to an underlying (liquid–liquid) critical point, the power-law exponents, ν and γ, should increase and reach maximum values as the system approaches the critical pressure[54,56,57]. In the case of the Ising model, the maximum values for the corresponding exponents are ν = 0.63 and γ = 1.24 with a ratio of ν/γ = 0.5[54,56,57]. Previous analysis of the power law exponents of those obtained experimentally supercooled water indicate that ratio of the exponents, ν/γ = 0.65, which is relatively close to the ratio ν/γ = 0.51 that would be expected exactly at a critical point. Analysis of the γ exponents obtained from MD simulations indicate that the various models examined (TIP4P/2005, SPCE, E3B3 and iAMOEBA) underestimate the γ values compared to the experiment[55].

Here we observe that the γ exponent in glycerol-water is lower than expected for the LLCP, indicating that the system is in the supercritical region and that this apparent critical behavior is associated with approaching the Widom line upon cooling[55]. In addition, the γ value for the glycerol-water solution (γ = 0.36 ± 0.02) is lower than pure water (γ = 0.40 ± 0.01) indicating possibly that glycerol partially suppresses the critical fluctuations, which is consistent with the relative reduction in the compressibility.

An important observation from Fig. 4A is the lack of any clear maximum in the $\kappa_T(T)$ of the glycerol-water solution (3.2% glycerol mole fraction) over the temperature range studied, T = 229.3–295 K (black solid line). Similarly, the $\xi(T)$ data of the glycerol-water solution, does not indicate a maximum (magenta solid line in Supplementary Fig. 5B). This is in contrast to the case of pure water, where experiments show a maximum in $\kappa_T(T)$, $\xi(T)$, and specific heat capacity $C_P(T)$, all at $T \approx$ 230 K (the maxima in $\kappa_T(T)$ is mild but can be observed in Fig. 4, red empty triangles; reproduced from ref. 7). In the case of pure water, the maxima in these properties are associated with the system crossing the Widom line upon isobaric cooling at ambient pressure[6]. We note, however, that the number of data points for the glycerol-water solution in Fig. 4A is smaller than the number of points available for pure water[7]. Therefore, more experiments are needed, at approximately T = 230 K, to confirm the absence of an κ_T-maximum in the glycerol-water solution (χ_g = 3.2% glycerol mole fraction). Nevertheless, it is clear that adding glycerol shifts the values of $\kappa_T(T)$ towards lower temperatures, and, as discussed below, the results from MD simulations strongly suggest that such a maximum is pushed to T < 230 K.

Figure 4B shows the $\kappa_T(T)$ of the glycerol-water solution and pure water calculated from MD simulations which allows us to get insight into lower temperatures. As discussed in the Methods section, $\kappa_T(T)$ is obtained by calculating the volume fluctuations in the system. The MD simulations reveal a maximum in the $\kappa_T(T)$ of the glycerol-water solution at T = 223 ± 1 K; see Fig. 4B (black open circles). A κ_T-maximum is also found in bulk water (red empty triangles; see below). We note that the overall magnitude of the isothermal compressibility enhancement upon cooling is suppressed in the MD simulations in comparison to the experiment (see also Supplementary Fig. 6B), a known limitation of the TIP4P/2005 and most water models[58].

In order to further explore whether the experimental $\kappa_T(T)$ data provide any indications of a maximum in the $\kappa_T(T)$, we analyze the goodness of fit for the power-law model, based on the coefficient of

Table 1 | Power-law fitting parameters for the $\kappa_T(T)$ and $\xi(T)$ of the glycerol-water solution (χ_g = 3.2% glycerol mole fraction) based on the experimental data shown in Fig. 4 and Supplementary Fig. 4B

Sample	γ	ν	ν/γ
Glycerol-water (χ_g = 3.2 mol%)	0.36 ± 0.02	0.26 ± 0.1	0.73 ± 0.4
Pure water[55]	0.40 ± 0.01	0.26 ± 0.3	0.65
Ising model[54]	1.2	0.6	0.5

The fitting parameters are defined in Eq. (2).

determination R^2. The power-law model predicts a divergence at $T = T_s$, where the $\kappa_T(T)$ would be infinite. Approaching the Widom line, it is expected that the $\kappa_T(T)$ would deviate from the power-law prediction in the proximity of the $\kappa_T(T)$ maximum[55]. Supplementary Fig. 8A shows the power-law fit for the experimental $\kappa_T(T)$ data, including the whole temperature range (dashed line) and by excluding the κ_T data point at $T = 230$ K (solid line). Based on the R^2, we observe that the best fit to power law is obtained by excluding the $\kappa_T(T)$ data point at $T = 230$ K (solid line). Hence, the data point for $\kappa_T(T)$ at $T = 230$ K deviates from the power-law behavior. We validate this approach by performing a similar analysis on the MD simulations, shown in Supplementary Fig. 8B. Again, we observe a similar behavior, whereby excluding the $\kappa_T(T)$ data at $T \leq 230$ K (solid line) provides a significantly better agreement ($R^2 = 0.992$) with a power law. The fit to all values of $\kappa_T(T)$ including the $T = 230$ K data point is shown by the dashed line ($R^2 = 0.936$). This result indicates that the $\kappa_T(T)$ data deviate from the power law at $T = 230$ K. We note that the data at $T = 220$ K deviate even further from the power-law behavior, as this is the temperature where the $\kappa_T(T)$ maximum is observed.

It should be noted here, that the deviation at $T \leq 230$ K appears larger for the MD simulation than in the experiment, likely due to limitations of the MD model. TIP4P/2005 model underestimates the amplitude of the $\kappa_T(T)$ maximum for pure water. Indeed, a shift in pressure results in better agreement between the results of MD simulations of TIP4P/2005 water and experiments which can be explained by considering that the location of the liquid–liquid critical point in TIP4P/2005 water is shifted, in the P–T plane, relative to the corresponding location of the liquid–liquid critical point of real water. This effect is also seen in the broader $\kappa_T(T)$ maximum of TIP4P/2005 water, compared to experiments[21], which implies that any deviation observed for the power-law behavior would be more significant for the simulation than the experimental data, as observed in Supplementary Fig. 8B.

A comparison of the MD simulations results shown in Fig. 4B indicates that the addition of glycerol (i) reduces the value of the maximum in $\kappa_T(T)$ and (ii) shifts the κ-maximum to lower temperatures. In particular, point (ii) is fully consistent with the experimental data shown in Fig. 4A, where the $\kappa(T)$ of the glycerol-water is always lower than that of pure water. This observation implies that adding glycerol shifts the Widom line of water to lower temperatures at ambient pressure. This also suggests that adding glycerol has a similar effect on water as increasing the pressure, disrupting the hydrogen-bond network of water[28]. However, we note that in pure water, increasing pressure also increases the maximum value of κ_T since the system is brought closer to the critical point pressure of water[55]. The observed smaller magnitude of the κ_T for the glycerol-water solution, compared to pure water, can be rationalized by considering that, unlike the external force of pressure, the water structure is disrupted locally by the presence of the glycerol molecules *within* the solution. The intercalating glycerol molecules can cause an additional confinement effect which can limit the size of correlated water domains and thereby suppress the magnitude of the density fluctuations.

Local structure index

To explore the local structure of water within the glycerol-water solution, we calculate the local structure index (*LSI*) of the water molecules in the system. The *LSI* describes the local structure around a central water oxygen atom in terms of the distances between neighboring oxygen atoms (see Methods section). High values of *LSI* indicate ordered structures with well-defined first and second hydration shells, while low values of *LSI* indicate disordered, collapsed structures with molecules populating the interstitial shell, in between the first and second hydration shells[59–61]. MD simulations of pure liquid water at room temperature and $P = 1$ bar exhibit a bimodal *LSI* distribution[14,61,62]: highly tetrahedral LDL-like molecules result to large values of *LSI* while

HDL-like molecules, characterized by populated first-interstitial shells, exhibit low values of *LSI*. Figure 5A shows the distribution of *LSI* values calculated from the MD simulations of the glycerol-water solution at different temperatures. To obtain well-defined *LSI* distributions, we remove the molecular intermolecular vibrational effects due to thermal fluctuations and evaluate the *LSI* at the inherent structures (potential energy minima) of the system (see Methods). We find that, as reported in MD simulations of pure water[14,61,62], the glycerol-water solutions exhibit temperature-dependent bimodal *LSI* distributions, with a local minimum at $LSI \approx 0.114$ Å^2. The peak located at $LSI < 0.114$ Å^2 corresponds to HDL-like water molecules and shrinks upon cooling, while the second peak located at $LSI > 0.114$ Å^2 corresponds to LDL-like water molecules and becomes more pronounced with decreasing temperatures. Figure 5B shows the fraction of HDL-like ($LSI \leq 0.114$ Å^2) and LDL-like molecules ($LSI > 0.114$ Å^2) calculated from Fig. 5A. At $T \approx 232$ K, the glycerol-water solution is composed of an equal amount of LDL- and HDL-like water molecules; at higher (lower) temperatures, the majority of the water molecules are HDL-like (LDL-like).

Snapshots of the glycerol-water solution extracted from our MD simulations are included in Fig. 5C for the cases $T = 190$ K (left), $T = 230$ K (center) and $T = 270$ K (right). Here, the glycerol molecules are colored in white, while the HDL- and LDL-like water molecules are shown in red and blue colors, color-coded based on their classification as HDL-like (with $LSI \leq 0.114$ Å^2) and LDL-like (with $LSI > 0.114$ Å^2), respectively. As expected, the system at $T = 190$ K is characterized by large cohesive LDL-like (blue) domains containing scattered glycerol molecules; a small number of residual HDL-like water molecules are also observed. The opposite scenario is observed at high temperatures; at $T = 270$ K, the system is composed mostly of HDL-like (red) molecules surrounded by scattered glycerol molecules and LDL-like domains. We note that, at $T = 270$ K, the relative difference between the HDL-like and LDL-like fraction of molecules is less pronounced than at $T = 190$ K, as observed before for pure water[61]. At $T = 232$ K, on the other hand, there are nearly equal fractions of HDL-like and LDL-like waters that form highly interpenetrating networks. The rather large percolation of the LDL and HDL domains throughout the system could reflect maximal fluctuations in the proximity to the Widom line. This observation closely coincides with previous simulations of pure water with the TIP4P/2005 model, where a 1:1 distribution between HDL- and LDL-like molecular species was observed at $T \approx 233$ K[61]. At $T = 230$ K, we observe that the LSI does not differ whether one examines the bulk water or that in the proximity of the glycerol (see Supplementary Supplementary Fig. 13). It should be noted here, as shown in ref. 63, that these results can depend on the local order parameter used to examine the nature of water in the hydration layer. Our study based on the LSI order parameter suggests that at $T = 230$ K, the local glycerol environment consists 1:1 of HDL/LDL water molecules, which reversely indicates that the system is isocompositional, i.e. LDL and HDL have the same concentration of glycerol, as suggested previously[28].

Discussion

In this work, we present results from femtosecond SAXS and WAXS experiments, and complementary MD simulations of dilute glycerol-water solutions ($\chi_g = 3.2\%$ glycerol mole fraction) over a wide range of temperatures, $T = 229.3$–295 K. By using rapidly evaporating microdroplets in vacuum (18.7 μm in diameter), we study the glycerol-water solutions deep in the supercooled liquid regime ($T = 229.3$ K), thereby avoiding crystallization. Overall, we find a good agreement between the SAXS/WAXS experiments and MD simulations. We observe that:

(i)   In the WAXS regime, the structure factor first-peak position $q_1(T)$ shifts towards lower values of momentum transfer q as the temperature decreases [Figs. 2, 3]. A similar temperature effect on $q_1(T)$ has been reported for pure water[7,9]. This implies that, as in the case of pure water, the local arrangements of the water molecules within the glycerol-water solution become more
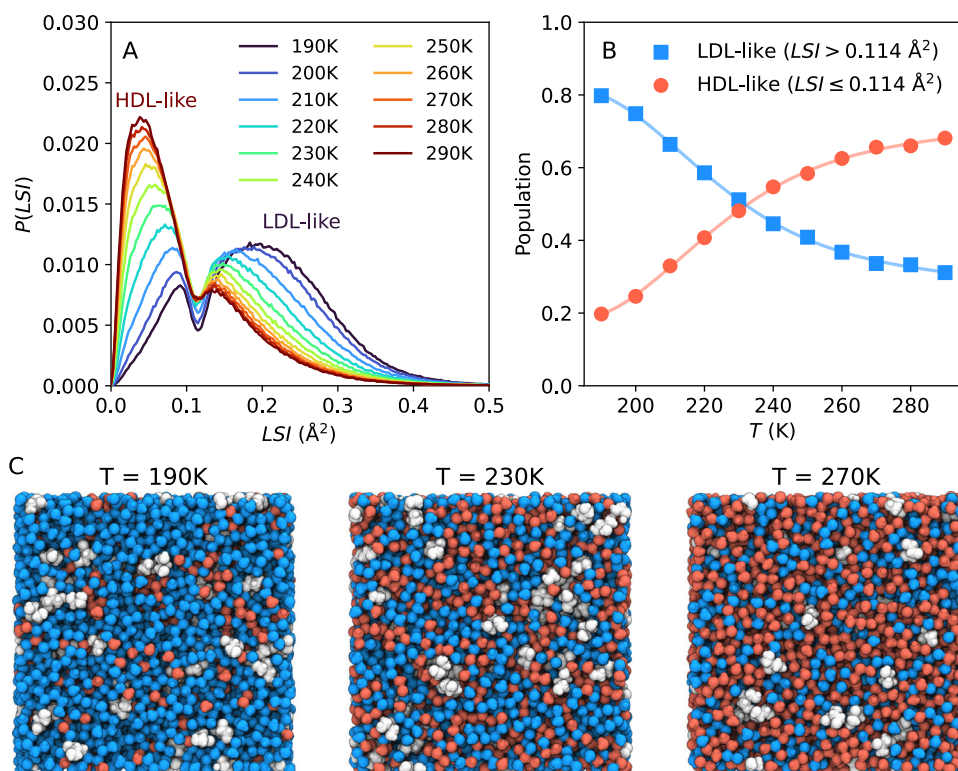
Fig. 5 | The inherent local structure index (LSI) of water from MD simulations of glycerol-water solution at different temperatures. A Probability distributions of the inherent LSI for the water molecules shown for different temperatures. The distribution is bimodal corresponding to HDL-like water molecules at $LSI < 0.114$ Å^2 and LDL-like water molecules for $LSI > 0.114$ Å^2. **B** The temperature dependence of the LSI populations, indicating a decrease of the HDL-like population (red circles, $LSI \leq 0.114$ Å^2) and an increase of the LDL-like population (blue squares, $LSI > 0.114$ Å^2) upon cooling. The population crossing occurs at approximately $T = 232$K. Solid lines correspond to smoothing spline fits. **C** Snapshots of the MD simulation box at $T = 190$ K (left), $T = 230$ K (center) and $T = 270$ K (right). Here, the water molecules are colored according to their inherent LSI value with HDL-like water in red ($LSI \leq 0.114$ Å^2) and LDL-like in blue ($LSI > 0.114$ Å^2), while glycerol molecules are shown in white. The simulation boxes were rendered using VMD[87].

ordered (tetrahedral) upon cooling [Fig. 5]. Interestingly, the temperature-derivative dq_1/dT obtained from the MD simulations of the glycerol-water solution and pure water exhibit a maximum at a similar temperature, $T \approx 230$ K. In the case of pure water, this temperature coincides approximately with the Widom line temperature (at ambient pressure)[7].

(ii) At very low q, in the SAXS regime, both experiments and MD simulations show a strong increase in the structure factor of the glycerol-water solution upon cooling. This implies that there is an anomalous increase in density fluctuations in the solution with decreasing temperature. From the SAXS experiments, we calculate the isothermal compressibility $\kappa_T(T)$ of the glycerol-water solution, and the correlation length of the associated density fluctuations, $\xi(T)$. Both quantities increase anomalously upon cooling following a power law. The corresponding power-law exponents are not large enough to justify the existence of a (liquid–liquid) critical point at ambient pressure. Instead, our results indicate that the microdroplets are in the supercritical state and are fully consistent with those from experiments performed for pure water[7,55].

An important experimental result of our study is that the addition of glycerol reduces the isothermal compressibility and the associated density fluctuations of pure water (at a given temperature); this could be, for example, due to the direct interactions (hydrogen-bonds formation) between the glycerol and water molecules, and/or because the glycerol molecules may limit the size of the density fluctuations (confinement effect). Additionally, our results indicate that adding glycerol shifts both the $\kappa_T(T)$ and $\xi(T)$ of pure water towards lower

temperatures. We note that the $\kappa_T(T)$ of pure water exhibits a maximum at $T \approx 230$ K while, instead, our studies on glycerol-water solutions ($\chi_g = 3.2\%$ glycerol mole fraction)) suggest that such a maximum, shifts to lower temperatures due to the presence of glycerol. Extending our experiments to lower temperatures, $T < 230$ K, to directly observe the maximum in $\kappa_T(T)$ is highly non-trivial. One possible avenue to extend the experimentally accessible temperatures to significantly lower values would be to utilize the high repetition rates of superconducting XFELs (like the European XFEL or LCLS-II), which allow the acquisition of data at kHz to MHz rates (vs 50Hz at SACLA). This approach would enable orders of magnitude more statistics even at very low hit-rates, which can be especially useful for accessing the regime $T < 230$ K, where the hit-rate is on the order of 0.1%. This comes with challenges related to operating the liquid jet at kHz to MHz rates, as well as big data volumes, which have been solved already for serial crystallography[64]. An alternative approach to explore the existence of an LLCP at elevated pressure would be to prepare high-density amorphous ice samples with different glycerol-water concentrations and perform a temperature-jump experiment (as in refs. 6,10,12). Possible challenges here relate to establishing accurately the trajectory across the pressure–temperature phase space and creating thin ice samples to ensure homogeneous heating.

The effects of glycerol on the κ_T-maximum of water are nicely demonstrated by our MD simulations which allows us to extend the temperature range accessible to the glycerol-water solution down to $T = 190$ K. The MD simulations reveal that a maximum in the $\kappa_T(T)$ of the glycerol-water solution indeed exists, and that it is shifted to lower temperatures relative to pure water. Specifically, the κ_T-maximum temperatures are $T = 223 \pm 1$ K for the glycerol-water solution and pure

water. In the case of pure water, the κ_T-maximum observed in experiments ($T \approx 230$ K[7]) and MD simulations (TIP4P/2005 $T \approx 234$ K[21]) was linked to density fluctuations between HDL/LDL domains, and the κ_T-maximum itself was identified as the Widom line[6,7,55,58] emanating from a LLCP. The same interpretation applies to the water domains within the glycerol-water solution; the role of glycerol is just to shift such LDL/HDL fluctuations to lower temperatures. Our results are further consistent with the previous MD simulations of ion-water mixtures, which indicate that the location of the LLCP in the phase diagram is shifted relative to pure bulk water due to the presence of the solutes[31–34].

The analysis of the LSI order parameter, based on the MD simulations, is also consistent with the presence of LDL and HDL domains in the glycerol-water solution. Specifically, we found that the fraction of LDL-like water molecules within the mixture increases upon cooling. Importantly, the MD simulations show that at $T \approx 232$ K the system is composed of equal amounts of HDL- and LDL-like molecules, similar to the the case of pure water. This observation indicates that even though the κ_T-maximum, reflecting collective density fluctuations, is shifted to lower temperatures in the glycerol-water solution ($T = 223 \pm 1$ K), the local water structure in the mixture follows the temperature dependence of pure water. This interpretation is consistent with the observed maximum of the temperature-derivative dq_1/dT at $T \approx 231$ K, as it is also a local structural probe. That can be an indication that the line in the phase space of the glycerol-water solution defined by the κ_T-maxima deviates from those defined by structural observables, such as the dq_1/dT and the HDL/LDL populations extracted with the LSI. The lines of maxima of different thermodynamic response functions, as well as dynamic and structural observables, can deviate from each other in the supercritical of the solution[65]. These lines of maxima of the different properties should, however, converge upon approaching the critical point into a single line, the Widom line, defined as the line of the maxima of the correlation length. Therefore, our data indicate that the system is in supercritical conditions at this region of the phase space (ambient pressure and approximately $T > 229$ K) and that if an LLCP exists in the glycerol-water mixture, it is expected to be located at higher concentrations and/or higher pressures than those studied here. This observation is in accordance with previous studies starting from glassy samples, which indicate an LLCP in the glycerol-water system at (T, χ_g, P) = (150 K, 13.5%, 45 MPa).

In conclusion, our results shed light on the influence of glycerol on the local structure of supercooled water and provide evidence that the two-liquid framework of water can be extended to describe the thermodynamic properties of solutions. Alternatively, our findings show how the properties of pure water, and its underlying LLCP, may affect the properties of aqueous solutions. We find that, even at dilute conditions, the presence of glycerol can partially suppress the collective density fluctuations of pure water and shift its LLCP towards lower temperatures. The suppression of density fluctuations observed here can be linked to glycerol's cryoprotectant ability to frustrate the fluctuations associated with the formation of the critical nucleus preceding crystallization of the system[66]. The knowledge of the changes in the local water structure and nanoscale fluctuations, with increasing glycerol content, as provided in the present study, are then potentially crucial to design the appropriate cryoprotectant mixtures. Our results may therefore be important to advance cryopreservation techniques and the design of cryoprotectants that better prevent ice nucleation, a key challenge in cryopreservation. By tuning glycerol concentrations, or combining it with other cryoprotectants like DMSO or ethylene glycol, formulations can be optimized to maximize the suppression of crystallization while maintaining low toxicity[27]. This is particularly relevant for biological applications where ice formation can damage cells and can be beneficial for cryopreserving complex tissues or organs, where ice formation must be avoided[26]. Additionally, understanding the impact of

Table 2 | XFEL experiment parameters

Photon energy	7.7 keV
Pulse energy	≈ 0.5 mJ
Pulse length	<10 fs
Repetition rate	30 Hz
Beam focus size (FWHM)	4.5×3 μm^2 (horizontal × vertical)
MPCCD octal SWD detector	4×2 units, 1024×512 pixels per unit
Pixel size	50 μm
Accessible q-range	$q \approx 0.15$-1.89 Å^{-1}

glycerol on water local structure at elevated pressure would benefit the development of high-pressure cryopreservation techniques in combination with glycerol-based solutions that could further enhance control over freezing processes[67].

Methods

X-ray free-electron laser (XFEL) measurements
The XFEL experiments were performed at the BL3 beamline (EH2 hutch) at the SPring-8 Angstrom Compact free electron LAser (SACLA) in Japan (proposal no. 2022B8033). The experimental parameters are summarized in Table 2.

Sample and droplet setup parameters
For the glycerol-water solution droplets setup, we follow a protocol similar to that employed in ref. 7 to study the properties of supercooled droplets of pure water. Here, we prepare liquid droplets of 18.7 μm in diameter composed of glycerol-water solutions of $\chi_g = 3.2\%$ glycerol mole fraction (14.5 wt%). We used MilliQ water and glycerol from Sigma-Aldrich (prod. no. G9012). The droplets are supercooled by the rapid evaporative cooling technique described in refs. 6,7,9,68. The droplets were generated using a piezo-driven microdispenser device with an orifice diameter of 10 μm- (MJ-ATP-01-10-8MX from Microfab), and modulated at frequency 156–157 kHz. A back pressure of 2.5–2.8 bar nitrogen gas was applied to the sample solution container to pump the liquid through the dispenser, creating a train of equidistant droplets with 85 μm center-to-center distance (see Fig. 1. The droplets were injected vertically downwards into a vacuum chamber at vacuum pressure 1.6 Pa and the jet was captured by a cryotrap. The sample vacuum chamber was directly connected to the X-ray flight tube downstream and with an 8-inch exit kapton window (125 mm thickness) at ≈ 95 mm from the X-ray interaction point. A beam stop (Tungsten-Aluminum-Graphite cylinder, 3 mm in diameter and 13 mm in length) was glued to the inside of the exit window to block the direct beam.

To study the properties of glycerol-water solution at different temperatures, data was collected from droplets at different distances from the dispenser tip. The position of the dispenser was controlled using a manipulator (VAb Vakuum-Anlagenbau GmbH). The temperature of the droplets, which decreases as they travel in vaccuum (evaporative coolingin the range $T = 229$–259 K) was estimated using the Knudsen evaporation theory and thermodynamic properties of glycerol-water mixtures. The Knudsen evaporation model for droplet temperature estimation has been examined in detail previously, both experimentally based on XFEL[7,9] and Raman[69] measurements, as well as from MD simulations[70] (see also Supplementary Note 3).

To monitor the position and characterize the droplet stream during the measurements, an optical microscope was focused on the X-ray focal point in the direction perpendicular to the optical axis. The droplet size and droplet-droplet distance were calibrated from the microscope images (see example in Fig. 1) close to the dispenser tip, and from the known outer diameter of the dispenser housing (565.4 μm), as determined from high-resolution optical microscopy.

WAXS and SAXS data analysis

For each temperature studied, about 20,000–200,000 single-shot images were collected, filtered (to exclude missed and frozen droplets), and averaged; see Supplementary Note 1. The procedures to obtain the structure factor $S(q)$ from the measured scattering intensity $I(q)$ are detailed in Supplementary Note 1. Note that the liquid structure factors presented herein are normalized to the molecular form factor $f(q)$, and hence represent the center-of-mass arrangement of liquid molecules in reciprocal space. The structure factor first-peak position $q_1(T)$ (in the WAXS patterns) was extracted by fitting a Gaussian function over the range $q \approx 1.7–1.9$ Å^{-1}. A similar fitting procedure was applied to obtain the q_1 structure factor peak positions from the XRD measurements and MD simulations of the glycerol-water solution, as well as from reference structure factor patterns of pure water in literature[7,53]. These data were fitted with Gaussian functions over a slightly larger accessible range $q \approx 1.7–2.1$ Å^{-1}.

The total SAXS structure factor $S(q)$ is analyzed by following the same procedure employed in ref. [7,50,51]. Specifically, $S(q)$ is decomposed as the sum of a normal liquid component, S_N, and an anomalous component, S_A,

$$S(q) = S_A(q) + S_N(q) \qquad (3)$$

The Percus-Yevick (PY) structure factor for a hard-sphere system, $S_{PY}(q)$, is used to describe the normal component of the structure factor, i.e., $S_N(q) = S_{PY}(q)$. We utilize the PY method provided by the *Jscatter* (1.6.4) package[71,72], $S_{PY}(q, R, \eta)$. The parameters R and η are the hard-sphere radius and the volume fraction of the system, respectively, and are obtained by fitting the SAXS curves for $0.15 < q < 0.7$ Å^{-1}. To minimize the number of fitting parameters we assume that R is temperature-independent ($R = 1.78 \pm 0.01$ Å); this assumption does not affect the resulting trends.

The excess anomalous scattering $S_A(q)$ is due to critical fluctuations and is described by the Ornstein-Zernike relation[54,57,73]; for a given temperature,

$$S_A(q) = \frac{S_A(0)}{1 + \xi^2 q^2}, \qquad (4)$$

where ξ is the correlation length and $S_A(0)$ is the excess anomalous scattering at $q = 0$. By fitting the $S(q)$ in the SAXS domain using Eq. (3), we additionally obtain the structure factor extrapolated at $q \to 0$, from which the isothermal compressibility of the solution is calculated via Eq. (1).

X-ray diffraction (XRD) measurements

X-ray diffraction (XRD) measurements of glycerol-water solutions ($\chi_g = 3.2\%$ glycerol mole fraction), made from the same batch solution used for the SACLA XFEL experiments, were conducted using a Bruker D8 VENTURE Single Crystal XRD with a Photon III detector and Mo (K-α) source. The solution was measured in Kapton capillaries (1 mm diameter) with a 70 mm sample-detector distance. The solutions were studied at temperatures ranging from $T = 295$ K to moderate supercooling $T = 250$ K using a liquid nitrogen-cooled air flow and a 15 min temperature equilibration time. The larger WAXS q-range ($q \approx 0.6$-6 Å^{-1}) acquired from the XRD measurements was utilized for the accurate normalization of the scattering intensity $I(q)$ to electron units, and conversion to the structure factor $S(q)$ for the SACLA XFEL scattering patterns, as described in Supplementary Note 1.

Molecular dynamics (MD) simulations

All MD simulations were performed using the GROMACS 2022.5 software package[74]. The CHARMM36 force field[75,76] was used to represent the glycerol molecules and the TIP4P/2005 model was used to model the water molecules[77]. The simulation box contains 320 and 9,680

molecules of glycerol and water, respectively, and the system box dimensions are approximately 69Å × 69Å × 69Å. Periodic boundary conditions apply along the three directions. The simulation time step is $dt = 2$ fs.

MD simulations are performed at $T = 190, 200, 210, . . . 290$ K. The equilibration of the system is done in two steps: (1) a short 10 ns MD simulation at constant volume (NVT), (ii) followed by another MD simulation performed at constant pressure (NPT) for 0.2–1.0 μs, depending on temperature (from 0.2 μs at $T = 290$ K to 2.0 μs at 190K). During equilibration, the temperature is controlled using a Nosé-Hoover thermostat (with a coupling time of 1 ps) while the pressure is kept constant using a Berendsen barostat (with a coupling time of 2 ps). The system is equilibrated at each temperature, independently by monitoring the time dependence of the potential energy (see Supplementary Note 5). At each temperature, equilibration is followed by a 200 ns production run at $P = 1$ bar (see Supplementary Note 5). During the production runs, the temperature and pressure are controlled by a Nosé-Hoover thermostat (with a coupling time of 1 ps) and a Parrinello-Rahman barostat (with a coupling time of 10 ps). This approach allows for efficient pre-equilibration due to the fast convergence of the Berendsen[78] barostat, whereas the Parrinello-Rahman barostat[79,80] combined with the Nosé-Hoover temperature coupling[81], allows to sample accurately density fluctuations as it gives the correct ensemble. The total production run time is longer than the time required for the density autocorrelation function to decay to zero (see Supplementary Fig. 11). Similarly, the total production time is long enough so that both the glycerol and water molecules reach the diffusive regime at which the corresponding mean-square displacement (MSD) increases linearly with time. In addition to checking for any possible sources of uncertainty due to the different starting geometries, we have repeated all simulations three times, starting from independent molecular geometries and repeating the equilibration and production runs, as described above (see Supplementary Note 5). Part of the calculations were performed in a reproducible environment using the Nix package manager together with NixOS-QChem[82].

Simulated X-ray structure factor

In the MD simulations, the X-ray structure factor $S(q)$ was calculated from the radial distribution function $g(r)$ according to the method described in ref. [22]. Specifically,

$$S(q) \simeq 1 + 4\pi\bar{\rho} \int_0^{r_{max}} w(r)r[g(r) - 1]\frac{\sin(qr)}{q}\,dr, \qquad (5)$$

where $\bar{\rho}$ is the number density and r is the radial distance. In Eq. (5) only the heavy atoms are used for the calculation of $g(r)$ (i.e., H atoms are excluded) since these atoms dominate the scattering cross-section at the experimental photon energies considered. The integration interval is limited to $r_{max} = a/2$ where a is the simulation box size. $w(r)$ is a window function introduced to minimize truncation ripples arising from the Fourier transform (Eq. (5)) over a limited integration interval; $w(r)$ is given by[22]

$$w(r) = \begin{cases} 1 - 3\left(\frac{r}{r_{max}}\right)^2, & r < \frac{1}{3}r_{max} \\ \frac{3}{2}\left[1 - \frac{2r}{r_{max}} + \left(\frac{r}{r_{max}}\right)^2\right], & \frac{1}{3}r_{max} < r < r_{max} \\ 0, & r > r_{max} \end{cases} \qquad (6)$$

Eq. (5) is valid in the dilute limit (see details in Supplementary Note 1) and is utilized here as an approximation for the dilute solution (3.2% glycerol mole fraction). For every temperature, the $g(r)$ is computed individually for each frame and then averaged over every 10 frames separated by 100 ps (in total 1 ns). From each averaged $g(r)$, a

corresponding $S(q)$ is determined. The standard error in the $S(q)$ is calculated over the whole production run (200 ns).

Isothermal compressibility from the MD simulations

The isothermal compressibility $\kappa_T(T)$ is calculated from the MD simulations by evaluating the volume fluctuations (δV) in the system during the production runs[74,83]. Specifically,

$$\kappa_T = \frac{\langle \delta V^2 \rangle_{NPT}}{k_B \langle V \rangle \langle T \rangle}, \tag{7}$$

where $\langle V \rangle$ is the time-averaged volume of the system, k_B is the Boltzmann constant, and $\langle T \rangle$ is the time-averaged temperature.

Calculation of the Local Structure Index (LSI)

For a given water molecule i, the corresponding local structure index (LSI_i) is given by[59–61]

$$LSI_i = \frac{1}{n_i} \sum_{j=1}^{n_i} \left[\Delta_{ij} - \langle \Delta_{ij} \rangle \right]^2, \tag{8}$$

where n_i is the number of water oxygen neighbors that molecule i has within a O−O cutoff distance $r_c^{OO} = 3.7$ Å. $\Delta_{i,j} = r_{i,j+1} - r_{i,j}$ where $r_{i,j}$ is the distance between the oxygen atoms of molecules i and j.

To improve the resolution of the distribution of LSI values of the different water molecules, we calculated the LSI parameter of the molecules at the so-called inherent structure[61]. For a given instantaneous configuration, sampled during the MD simulation, the inherent structure is the corresponding configuration obtained by minimization of the potential energy of the system. For a given temperature, we obtained 101 configurations evenly sampled from the production run. Potential energy minimization of these configurations was performed using the steepest descent algorithm. The system is considered to reach its inherent structure when the maximum force (gradient in the potential) during the minimization algorithm is smaller than 50 kJ mol^{-1} nm^{-1}.

Data availability

The data are available from the authors upon request. Source data are provided with this paper.

References

1. Debenedetti, P. G. Supercooled and glassy water. *J. Phys.: Condens. Matter* **15**, R1669 (2003).
2. Debenedetti, P. G. & Stanley, H. E. Supercooled and glassy water. *Phys. Today* **56**, 40–46 (2003).
3. Nilsson, A. & Pettersson, L. G. The structural origin of anomalous properties of liquid water. *Nat. Commun.* **6**, 8998 (2015).
4. Handle, P. H., Loerting, T. & Sciortino, F. Supercooled and glassy water: metastable liquid(s), amorphous solid(s), and a no-man's land. *Proc. Natl Acad. Sci. USA* **114**, 13336–13344 (2017).
5. Speedy, R. J. & Angell, C. A. Isothermal compressibility of supercooled water and evidence for a thermodynamic singularity at -45˚C. *J. Chem. Phys.* **65**, 851 (1976).
6. Pathak, H. et al. Enhancement and maximum in the isobaric specific-heat capacity measurements of deeply supercooled water using ultrafast calorimetry. *Proc. Natl Acad. Sci. USA* **118**, e2018379118 (2021).
7. Kim, K. H. et al. Maxima in the thermodynamic response and correlation functions of deeply supercooled water. *Science* **358**, 1589 (2017).
8. Poole, P. H., Sciortino, F., Essmann, U. & Stanley, H. E. Phase behaviour of metastable water. *Nature* **360**, 324 (1992).
9. Sellberg, J. A. et al. Ultrafast X-ray probing of water structure below the homogeneous ice nucleation temperature. *Nature* **510**, 381 (2014).
10. Kim, K. H. et al. Experimental observation of the liquid-liquid transition in bulk supercooled water under pressure. *Science* **370**, 978 (2020).
11. Perakis, F. et al. Diffusive dynamics during the high-To-low density transition in amorphous ice. *Proc. Natl Acad. Sci. USA* **114**, 8193–8198 (2017).
12. Amann-Winkel, K. et al. Liquid-liquid phase separation in supercooled water from ultrafast heating of low-density amorphous ice. *Nat. Commun.* **14**, 442 (2023).
13. Debenedetti, P. G. & Stillinger, F. H. Supercooled liquids and the glass transition. *Nature* **410**, 259 (2001).
14. Palmer, J. C. et al. Metastable liquid-liquid transition in a molecular model of water. *Nature* **510**, 385 (2014).
15. Debenedetti, P. G., Sciortino, F. & Zerze, G. H. Second critical point in two realistic models of water. *Science* **369**, 289 (2020).
16. Mishima, O. & Stanley, H. E. The relationship between liquid, supercooled and glassy water. *Nature* **396**, 329–335 (1998).
17. Mishima, O. Volume of supercooled water under pressure and the liquid-liquid critical point. *J. Chem. Phys.* **133**, 144503 (2010).
18. Nilsson, A. Origin of the anomalous properties in supercooled water based on experimental probing inside "no-man's land". *J. Non-Cryst. Solids X* **14**, 100095 (2022).
19. Amann-Winkel, K. et al. X-ray and neutron scattering of water. *Chem. Rev.* **116**, 7570–7589 (2016).
20. Xu, L. et al. Relation between the Widom line and the dynamic crossover in systems with a liquid-liquid phase transition. *Proc. Natl Acad. Sci. USA* **102**, 16558–16562 (2005).
21. Abascal, J. L. F. & Vega, C. Widom line and the liquid-liquid critical point for the TIP4P/2005 water model. *J. Chem. Phys.* **133**, 234502 (2010).
22. Wikfeldt, K. T., Huang, C., Nilsson, A. & Pettersson, L. G. M. Enhanced small-angle scattering connected to the Widom line in simulations of supercooled water. *J. Chem. Phys.* **134**, 214506 (2011).
23. Hestand, N. J. & Skinner, J. L. Perspective: Crossing the Widom line in no man's land: experiments, simulations, and the location of the liquid-liquid critical point in supercooled water. *J. Chem. Phys.* **149**, 140901 (2018).
24. Weis, J., Sciortino, F., Panagiotopoulos, A. Z. & Debenedetti, P. G. Liquid-liquid criticality in the WAIL water model. *J. Chem. Phys.* **157**, 024502 (2022).
25. Gartner, T. E. et al. Signatures of a liquid-liquid transition in an ab initio deep neural network model for water. *Proc. Natl Acad. Sci. USA* **117**, 26040–26046 (2020).
26. Whaley, D. et al. Cryopreservation: an overview of principles and cell-specific considerations. *Cell Transplant.* **30**, 0963689721999617 (2021).
27. Murray, K. A. & Gibson, M. I. Chemical approaches to cryopreservation. *Nat. Rev. Chem.* **6**, 579–593 (2022).
28. Murata, K. & Tanaka, H. Liquid-liquid transition without macroscopic phase separation in a water-glycerol mixture. *Nat. Mater.* **11**, 436 (2012).
29. Murata, K. & Tanaka, H. General nature of liquid-liquid transition in aqueous organic solutions. *Nat. Commun.* **4**, 1–8 (2013).
30. Woutersen, S., Ensing, B., Hilbers, M., Zhao, Z. & Angell, C. A. A liquid-liquid transition in supercooled aqueous solution related to the HDA-LDA transition. *Science* **359**, 1127–1131 (2018).
31. Corradini, D. & Gallo, P. Liquid-liquid coexistence in NaCl aqueous solutions: a simulation study of concentration effects. *J. Phys. Chem. B* **115**, 14161–14166 (2011).
32. Perin, L. & Gallo, P. Phase diagram of aqueous solutions of LiCl: a study of concentration effects on the anomalies of water. *J. Phys. Chem. B* **127**, 4613–4622 (2023).
33. Le, L. & Molinero, V. Nanophase segregation in supercooled aqueous solutions and their glasses driven by the polyamorphism of water. *J. Phys. Chem. A* **115**, 5900–5907 (2011).

34. Biddle, J. W., Holten, V. & Anisimov, M. A. Behavior of supercooled aqueous solutions stemming from hidden liquid-liquid transition in water. *J. Chem. Phys.* **141**, 074504 (2014).

35. Suzuki, Y. & Mishima, O. Two distinct Raman profiles of glassy dilute LiCl solution. *Phys. Rev. Lett.* **85**, 1322–1325 (2000).

36. Giebelmann, J., Bachler, J. & Loerting, T. Glass polymorphism in hyperquenched aqueous LiCl solutions. *J. Phys. Chem. B* **127**, 3463–3477 (2023).

37. Kobayashi, M. & Tanaka, H. Relationship between the phase diagram, the glass-forming ability, and the fragility of a water/salt mixture. *J. Phys. Chem. B* **115**, 14077–14090 (2011).

38. Kobayashi, M. & Tanaka, H. Possible link of the V-shaped phase diagram to the glass-forming ability and fragility in a water-salt mixture. *Phys. Rev. Lett.* **106**, 125703 (2011).

39. Loerting, T. & Giovambattista, N. Amorphous ices: experiments and numerical simulations. *J. Condens. Matter Phys.* **18**, R919–R977 (2006).

40. Suzuki, Y. & Mishima, O. Experimentally proven liquid-liquid critical point of dilute glycerol-water solution at 150 K. *J. Chem. Phys.* **141**, 094505 (2014).

41. Popov, I., Greenbaum Gutina, A., Sokolov, A. P. & Feldman, Y. The puzzling first-order phase transition in water-glycerol mixtures. *Phys. Chem. Chem. Phys.* **17**, 18063–18071 (2015).

42. Bachler, J. et al. Glass polymorphism in glycerol-water mixtures: II. Experimental studies. *Phys. Chem. Chem. Phys.* **18**, 11058–11068 (2016).

43. Jahn, D. A., Wong, J., Bachler, J., Loerting, T. & Giovambattista, N. Glass polymorphism in glycerol-water mixtures: I. A computer simulation study. *Phys. Chem. Chem. Phys.* **18**, 11042–11057 (2016).

44. Alba-Simionesco, C. et al. Interplay of vitrification and ice formation in a cryoprotectant aqueous solution at low temperature. *Proc. Natl Acad. Sci. USA* **119**, e2112248119 (2022).

45. Bruijn, J. R., van der Loop, T. H. & Woutersen, S. Changing hydrogen-bond structure during an aqueous liquid-liquid transition investigated with time-resolved and two-dimensional vibrational spectroscopy. *J. Phys. Chem. Lett.* **7**, 795–799 (2016).

46. Mallamace, F. et al. Some considerations on the transport properties of water-glycerol suspensions. *J. Chem. Phys* **144**, 014501 (2016).

47. Koop, T., Luo, B., Tsias, A. & Peter, T. Water activity as the determinant for homogeneous ice nucleation in aqueous solutions. *Nature* **406** (2000).

48. Bachler, J., Fidler, L.-R. & Loerting, T. Absence of the liquid-liquid phase transition in aqueous ionic liquids. *Phys. Rev. E* **102**, 060601 (2020).

49. Pathak, H. et al. Temperature dependent anomalous fluctuations in water: shift of ≈1 kbar between experiment and classical force field simulations. *Mol. Phys.* **117**, 3232–3240 (2019).

50. Huang, C. et al. The inhomogeneous structure of water at ambient conditions. *Proc. Natl Acad. Sci. USA* **106**, 15214–15218 (2009).

51. Huang, C. et al. Increasing correlation length in bulk supercooled H2O, D2O, and NaCl solution determined from small angle x-ray scattering. *J. Chem. Phys.* **133**, 134504 (2010).

52. Espinosa, J. R., Abascal, J. L. F., Sedano, L. F., Sanz, E. & Vega, C. On the possible locus of the liquid-liquid critical point in real water from studies of supercooled water using the TIP4P/Ice model. *J. Chem. Phys* **158**, 204505 (2023).

53. Skinner, L. B., Benmore, C. J., Neuefeind, J. C. & Parise, J. B. The structure of water around the compressibility minimum. *J. Chem. Phys.* **141**, 214507 (2014).

54. Eugene Stanley, H. *Introduction to Phase Transitions and Critical Phenomena* (Oxford University Press, 1971).

55. Späh, A. et al. Apparent power-law behavior of water's isothermal compressibility and correlation length upon supercooling. *Phys. Chem. Chem. Phys.* **21**, 26–31 (2018).

56. Sengers, J. V. & Shanks, J. G. Experimental critical-exponent values for fluids. *J. Stat. Phys.* **137**, 857–877 (2009).

57. Sheyfer, D. et al. Nanoscale critical phenomena in a complex fluid studied by x-ray photon correlation spectroscopy. *Phys. Rev. Lett.* **125**, 125504 (2020).

58. Pathak, H. et al. The structural validity of various thermodynamical models of supercooled water. *J. Chem. Phys.* **145**, 134507 (2016).

59. Shiratani, E. & Sasai, M. Growth and collapse of structural patterns in the hydrogen bond network in liquid water. *J. Chem. Phys.* **104**, 7671–7680 (1996).

60. Shiratani, E. & Sasai, M. Molecular scale precursor of the liquid-liquid phase transition of water. *J. Chem. Phys.* **108**, 3264–3276 (1998).

61. Wikfeldt, K. T., Nilsson, A. & Pettersson, L. G. M. Spatially inhomogeneous bimodal inherent structure of simulated liquid water. *Phys. Chem. Chem. Phys.* **13**, 19918–19924 (2011).

62. Camisasca, G., Galamba, N., Wikfeldt, K. T. & Pettersson, L. G. M. Translational and rotational dynamics of high and low density TIP4P/2005 water. *J. Chem. Phys.* **150**, 224507 (2019).

63. Camisasca, G., Tenuzzo, L. & Gallo, P. Protein hydration water: Focus on low density and high density local structures upon cooling. **370**, 120962.

64. Holmes, S. et al. Megahertz pulse trains enable multi-hit serial femtosecond crystallography experiments at x-ray free electron lasers. *Nat. Commun.* **13**, 4708 (2022).

65. Gallo, P., Corradini, D. & Rovere, M. Widom line and dynamical crossovers as routes to understand supercritical water. *Nat. Commun.* **5**, 5806 (2014).

66. Fitzner, M., Sosso, G. C., Pietrucci, F., Pipolo, S. & Michaelides, A. Pre-critical fluctuations and what they disclose about heterogeneous crystal nucleation. *Nat. Commun.* **8**, 2257 (2017).

67. Dahl, R. & Staehelin, L. A. High-pressure freezing for the preservation of biological structure: Theory and practice. *J. Electron Microsc. Tech.* **13**, 165–174 (1989).

68. Perakis, F. et al. Coherent X-rays reveal the influence of cage effects on ultrafast water dynamics. *Nat. Commun.* **9**, 1917 (2018).

69. Goy, C. et al. Shrinking of rapidly evaporating water microdroplets reveals their extreme supercooling. *Phys. Rev. Lett.* **120**, 015501 (2018).

70. Schlesinger, D., Sellberg, J. A., Nilsson, A. & Pettersson, L. G. M. Evaporative cooling of microscopic water droplets in vacuo: molecular dynamics simulations and kinetic gas theory. *J. Chem. Phys.* **144**, 124502 (2016).

71. Biehl, R. Jscatter, a program for evaluation and analysis of experimental data. *PLoS ONE* **14**, e0218789 (2019).

72. Kinning, D. J. & Thomas, E. L. Hard-sphere interactions between spherical domains in diblock copolymers. *Macromolecules* **17**, 1712–1718 (1984).

73. Chen, S. H., Lin, T. L. & Kotlarchyk, M. in *Surfactants in Solution* Vol. 6 (eds Mittal, K. L. & Bothorel, P.) 1315–1330 (Springer, 1986).

74. Abraham, M. J. et al. GROMACS: High performance molecular simulations through multi-level parallelism from laptops to supercomputers. *SoftwareX* **1-2**, 19–25 (2015).

75. Vanommeslaeghe, K. et al. CHARMM general force field: a force field for drug-like molecules compatible with the CHARMM all-atom additive biological force fields. *J. Comput. Chem.* **31**, 671–690 (2010).

76. Reiling, S., Schlenkrich, M. & Brickmann, J. Force field parameters for carbohydrates. *J. Comput. Chem.* **17**, 450–468 (1996).

77. Abascal, J. L. F. & Vega, C. A general purpose model for the condensed phases of water: Tip4p/2005. *J. Chem. Phys.* **123**, 234505 (2005).

78. Berendsen, H. J. C., Postma, J. P. M., van Gunsteren, W. F., DiNola, A. & Haak, J. R. Molecular dynamics with coupling to an external bath. *J. Chem. Phys.* **81**, 3684–3690 (1984).

79. Parrinello, M. & Rahman, A. Polymorphic transitions in single crystals: a new molecular dynamics method. *J. Appl. Phys.* **52**, 7182–7190 (1981).

80. Nosé, S. & Klein, M. Constant pressure molecular dynamics for molecular systems. *Mol. Phys.* **50**, 1055–1076 (1983).

81. Nosé, S. A molecular dynamics method for simulations in the canonical ensemble. *Mol. Phys.* **52**, 255–268 (1984).

82. Kowalewski, M. & Seeber, P. Sustainable packaging of quantum chemistry software with the nix package manager. *Int. J. Quant. Chem.* **122**, e26872 (2022).

83. Allen, M. P. & Tildesley, D. J.*Computer simulation of liquids* (Oxford, United Kingdom, 2017), second edition edn.

84. Mariedahl, D. et al. X-ray studies of the transformation from high- to low-density amorphous water. *Philos. Trans. R. Soc. A* **377**, 20180164 (2019).

85. Handle, P. H., Sciortino, F. & Giovambattista, N. Glass polymorphism in TIP4P/2005 water: a description based on the potential energy landscape formalism. *J. Chem. Phys.* **150**, 244506 (2019)

86. Bresme, F., Biddle, J. W., Sengers, J. V. & Anisimov, M. A. Minimum in the thermal conductivity of supercooled water: a computer simulation study. *J. Chem. Phys.* **140**, 161104 (2014).

87. Humphrey, W., Dalke, A. & Schulten, K. VMD—visual molecular dynamics. *J. Mol. Graph* **14**, 33–38 (1996).

Competing interests

The authors declare no competing interests.

Additional information

Supplementary information The online version contains supplementary material available at https://doi.org/10.1038/s41467-024-54890-y.

Correspondence and requests for materials should be addressed to Fivos Perakis.

Peer review information *Nature Communications* thanks the anonymous reviewer(s) for their contribution to the peer review of this work. A peer review file is available.

Reprints and permissions information is available at http://www.nature.com/reprints

Publisher's note Springer Nature remains neutral with regard to jurisdictional claims in published maps and institutional affiliations.

Supplementary information:

Supercritical density fluctuations and structural heterogeneity in supercooled water-glycerol microdroplets

Sharon Berkowicz[1,*], Iasonas Andronis[1,*], Anita Girelli[1], Mariia Filianina[1], Maddalena Bin[1], Kyeongmin Nam[2], Myeongsik Shin[2], Markus Kowalewski[1], Tetsuo Katayama[3,4], Nicolas Giovambattista[5,6], Kyung Hwan Kim[2], and Fivos Perakis[1,†]

[1]Department of Physics, AlbaNova University Center, Stockholm University, SE-10691 Stockholm, Sweden

[2]Department of Chemistry, Pohang University of Science and Technology (POSTECH), Pohang 37673, Republic of Korea

[3]Japan Synchrotron Radiation Research Institute, Kouto 1-1-1, Sayo, Hyogo 679-5198, Japan

[4]RIKEN SPring-8 Center, Kouto 1-1-1, Sayo, Hyogo 679-5148, Japan

[5]Department of Physics, Brooklyn College of the City University of New York, Brooklyn, NY 11210, USA.

[6]The Graduate Center of the City University of New York, New York, NY 10016, USA.

[*]These authors contributed equally.

[†]Email: f.perakis@fysik.su.se

Supplementary Note 1 The structure factor for a multi-component molecular liquid

The coherent scattering intensity $I(\mathbf{q})$ for a multi-molecular liquid can be written as [1]

$$I(\mathbf{q}) = \sum_n^N \sum_m^N f_n(\mathbf{q}) f_m(\mathbf{q}) e^{i\mathbf{q}\cdot(\mathbf{r}_n - \mathbf{r}_m)}, \tag{S1}$$

where $f_n(\mathbf{q})$ is the molecular form factor, $\mathbf{r}_n$ is the center of mass position of molecule n, and N is the number of molecules. Separation of the above expression into terms $n = m$ (self-scattering term, I_{self}) and $n \neq m$ (cross-term, I_{cross}) yields

$$I(\mathbf{q}) = \sum_n^N f_n^2(\mathbf{q}) + \sum_n^N \sum_{m \neq n}^N f_n(\mathbf{q}) f_m(\mathbf{q}) e^{i\mathbf{q}\cdot(\mathbf{r}_n - \mathbf{r}_m)} = N I_{self}(\mathbf{q}) + I_{cross}(\mathbf{q}). \tag{S2}$$

In addition, one can rewrite the self-term as a sum of self-terms for each molecular species j, summing over the total number of species J in the solution:

$$N I_{self}(q) = \sum_j^J N_j f_j^2(q) = N \sum_j^J x_j f_j^2(q), \tag{S3}$$

where N_j is the number of molecules of species j and $x_j = N_j/N$ is the corresponding molar fraction. Note that averaging over the azimuthal angle allows to drop the vector notation. Specifically, in the case of glycerol-water solution we have

$$I_{self}(q) = x_w f_w^2(q) + x_g f_g^2(q), \tag{S4}$$

where the subscripts w and g denote water and glycerol, respectively.

The structure factor $S(q)$ is defined as the coherently scattered intensity per molecule normalized by the self-scattering intensity of the independent molecules [1], i.e.

$$S(q) = \frac{I(q)}{N I_{self}(q)} = 1 + \frac{I_{cross}(q)}{N I_{self}(q)}, \tag{S5}$$
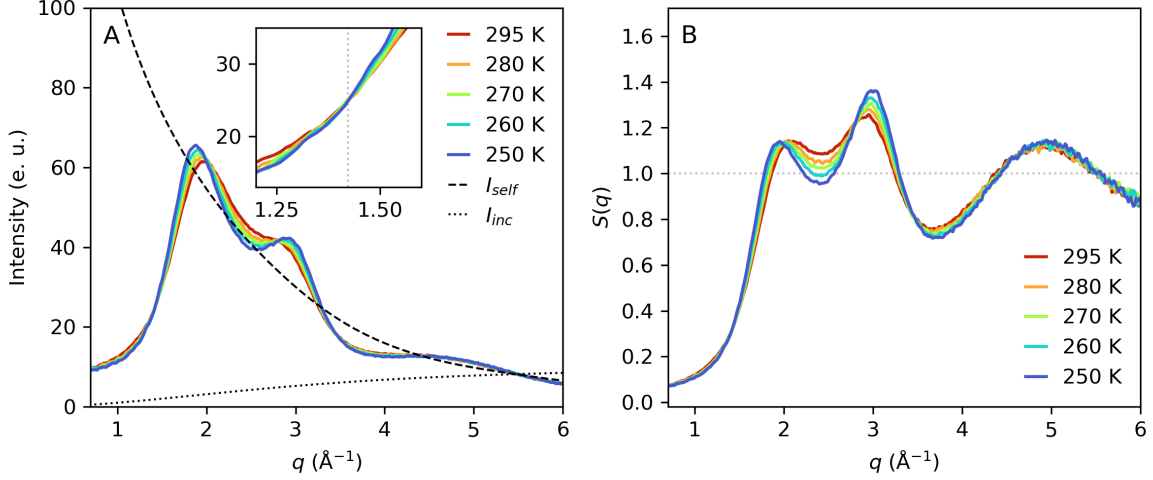
which oscillates around $S(q) = 1$. The structure factor is then calculated from the experimental data as

$$S(q) = \frac{\alpha I_{corr}(q) - I_{inc}(q)}{I_{self}(q)}, \tag{S6}$$

where $I_{corr}(q)$ is the corrected total X-ray scattering and $I_{inc}(q) = x_w I_{inc,w}(q) + x_g I_{inc,g}(q)$ is the incoherent (Compton) scattering intensity from glycerol-water solution. The coefficient α is introduced to normalize the corrected scattering intensity to electron units (per molecule) and determined by the Krogh-Moe method [2, 3]:

$$\alpha = \frac{\int_{q_1}^{q_2} (I_{self}(q) + I_{inc}(q)) q^2 dq - 2\pi^2 \rho Z^2}{\int_{q_1}^{q_2} I_{corr}(q) q^2 dq}, \tag{S7}$$

where ρ is the average number density of molecules (independent of the species) and $Z = x_w Z_w + x_g Z_g$
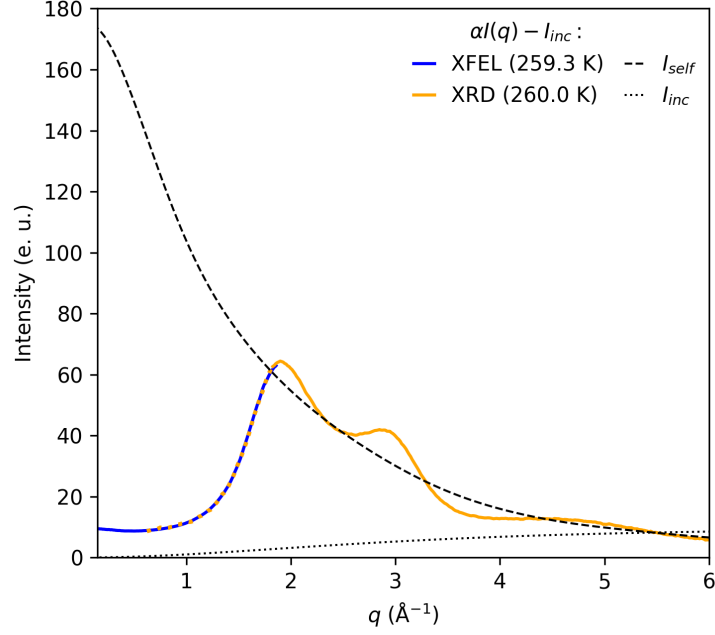
Supplementary Figure. 1 | X-ray diffraction (XRD) measurements of glycerol-water bulk solution ($\chi_g = 3.2\%$ glycerol mole fraction) in a 1-mm thick capillary at different temperatures. (A) The background-subtracted and solid-angle corrected scattering intensity scaled to electron units, i.e. $\alpha I_{corr}(q) - I_{inc}(q)$, using the Krogh-Moe method in Eq. (S7) [2, 3]. $I_{self}(q)$ is the self-scattering term (dashed line) and $I_{inc}(q)$ is the incoherent (Compton) scattering from glycerol-water solution (dotted line). The inset in A shows a zoom-in around the isosbestic point at $q \approx 1.43$ Å^{-1} (gray dotted line) used for normalization of the scattering intensities measured by ultrafast X-ray scattering at SACLA XFEL. (B) The obtained structure factor according to Eq. S6.

is the weighted average number of electrons of water and glycerol. The lower and upper integration limits used are $q_1 = 0.7$ Å^{-1} and $q_2 = 5.9$ Å^{-1}, respectively.

Table-top XRD measurements of glycerol-water bulk solution ($\chi_g = 3.2\%$ glycerol mole fraction) at temperatures $T = 260 - 295$ K are presented in Supplementary Figure 1, where the elastic scattering intensity is scaled to electron units and the structure factors are extracted using Eq. S6-S7.

Supplementary Note 1.1 Scattering intensity corrections

The corrected X-ray scattering $I_{corr}(q)$ was obtained from the measured scattering intensity $I_{meas}(q)$ of supercooled glycerol-water droplets following a number of corrections, including angular integration with solid-angle corrections (using the *Jscatter* software package [4]), sample transmission- and beam polarization corrections and background subtraction. For the scattering intensity of evaporatively cooled droplets recorded at SACLA XFEL, these corrections further included a filtering step to exclude X-ray shots of frozen droplets and missed X-ray shot targets, and averaging of scattering patterns recorded at the same conditions. As background in this case, we utilized the average scattering intensity of the missed X-ray shot targets. To account for small remaining noise (e.g. from variation of X-ray pulse characteristics between shots and exact path of the X-ray beam through the droplet), the background-subtracted average scattering intensities were normalized at the isosbestic point at $q \approx 1.43$ Å^{-1}, as determined by the standard XRD measurements of the same glycerol-water bulk solution ($\chi_g = 3.2\%$ glycerol mole fraction, see inset, Supplementary Figure 1A). In addition, since the scattering patterns measured at SACLA XFEL has a limited q-range (~ 0.15–1.89 Å^{-1}), we determined the Krogh-Moe coefficient α from the XRD measurements, and scaled the corrected XFEL scattering intensity accordingly to overlap with the XRD intensity at the common temperature of $T \approx 260$ K, as shown in Supplementary Figure 2.

Supplementary Figure. 2 | Comparison of the coherent scattering intensity (in electron units, e.u.) at $T \approx 260$ **K.** The intensities were measured by ultrafast X-ray scattering at SACLA X-ray free-electron laser (XFEL, blue solid line) and by X-ray diffraction (XRD, orange solid line) with a Mo (K-α) source. The incoherent scattering (dotted line) has been subtracted from the corrected total scattering intensity, i.e. $\alpha I_{corr}(q) - I_{inc}$ where $I_{inc} = x_w I_{inc,w} + x_g I_{inc,g}$ and α is the Krogh-Moe scaling coefficient [2, 3], such that the remaining elastic scattering intensity oscillates around the self-scattering from independent molecules (dashed line), $I_{self} = x_w f_w^2 + x_g f_g^2$.

Supplementary Note 1.2 Molecular form factors and incoherent scattering intensity for glycerol and water

For the individual contributions of water and glycerol to the concentration-weighted molecular form factor (Eq. (S4)) and incoherent scattering for the glycerol-water mixture, we have used the following approximations: (i) for water, we used the molecular form factor f_w and incoherent scattering intensity $I_{inc,w}$ from quantum chemical calculations in Ref. [5], as utilized in a previous experiment on pure water [6]. (ii) For glycerol, however, we calculated the molecular form factor f_g from the average energy-minimized conformation for a single glycerol molecule using the Debye-scattering formula [1]

$$|f(q)|^2 = \sum_n \sum_m f_n^a(q) f_m^a(q) \frac{\sin{(qr_{nm})}}{qr_{nm}}, \tag{S8}$$

which accounts for orientational averaging. Here, f refers to the molecular form factor as above while f_n^a refers to the atomic form factor for atom n; r_{nm} is the distance between atom n and m. In addition, we approximated the incoherent scattering intensity from glycerol $I_{inc,g}$ as a sum of the independent atomic contributions, i.e.

$$I_{inc} = \sum_n I_{inc,n}^a, \tag{S9}$$

where $I_{inc,n}^a$ is the incoherent scattering intensity from atom n. For the atomic form factors as well as for the atomic incoherent scattering intensities, we utilized tabulated values from Ref. [7].

4

Supplementary Note 1.3 Calculation of the structure factor from the radial distribution function

The scattering intensity of a liquid (Eq. S2) arising from short-range order can be expressed in terms of the deviation of the local number density $\rho(\mathbf{r})$ from the average density $\bar{\rho}$ [1] as follows

$$I(\mathbf{q}) = NI_{self}(\mathbf{q}) + \sum_n^N \int_V f_n(\mathbf{q})f_m(\mathbf{q})[\rho(\mathbf{r}_{nm}) - \bar{\rho}]e^{i\mathbf{q}\cdot(\mathbf{r_n}-\mathbf{r_m})}dV_m \ , \tag{S10}$$

where $\rho(\mathbf{r}_{nm})$ refers to the local number density in volume-element dV_m at position $\mathbf{r}_m$ with respect to the reference position $\mathbf{r}_n$. Averaging over reference positions yields

$$I(\mathbf{q}) = NI_{self}(\mathbf{q}) + N\langle f(\mathbf{q})\rangle^2 \int_V [\rho(\mathbf{r}) - \bar{\rho}]e^{i\mathbf{q}\cdot\mathbf{r}}dV \ , \tag{S11}$$
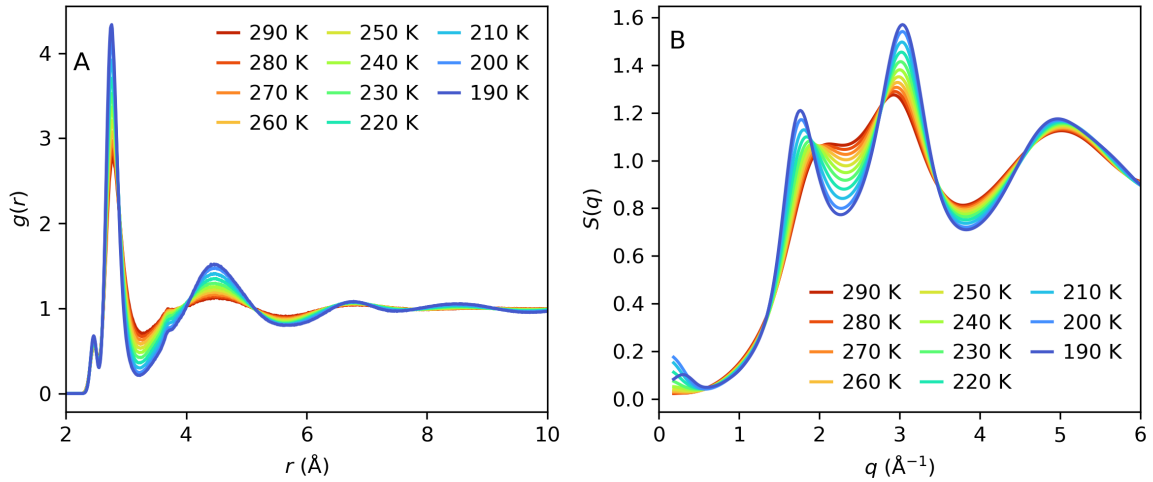
where we assumed an average scattering amplitude for each pair of molecules (n and m), i.e. $f_n(\mathbf{q})f_m(\mathbf{q}) \simeq \langle f(\mathbf{q})\rangle^2$. Further averaging over the azimuthal angle then yields

$$I(q) = NI_{self}(q) + N\langle f(q)\rangle^2 \int_0^\infty \bar{\rho}[g(r) - 1]\frac{\sin(qr)}{qr}4\pi r^2 \ dr \ . \tag{S12}$$

where $g(r) = \rho(r)/\bar{\rho}$ is the radial distribution function.

In the dilute limit we can assume that $\langle f(q)\rangle^2 = (\sum_j^J x_j f_j)^2 \simeq \sum_j^J x_j f_j^2(q) = I_{self}$. Thus, according to Eq. S5, the structure factor describing the short-range order of a dilute or single-component solution can be expressed as [1]
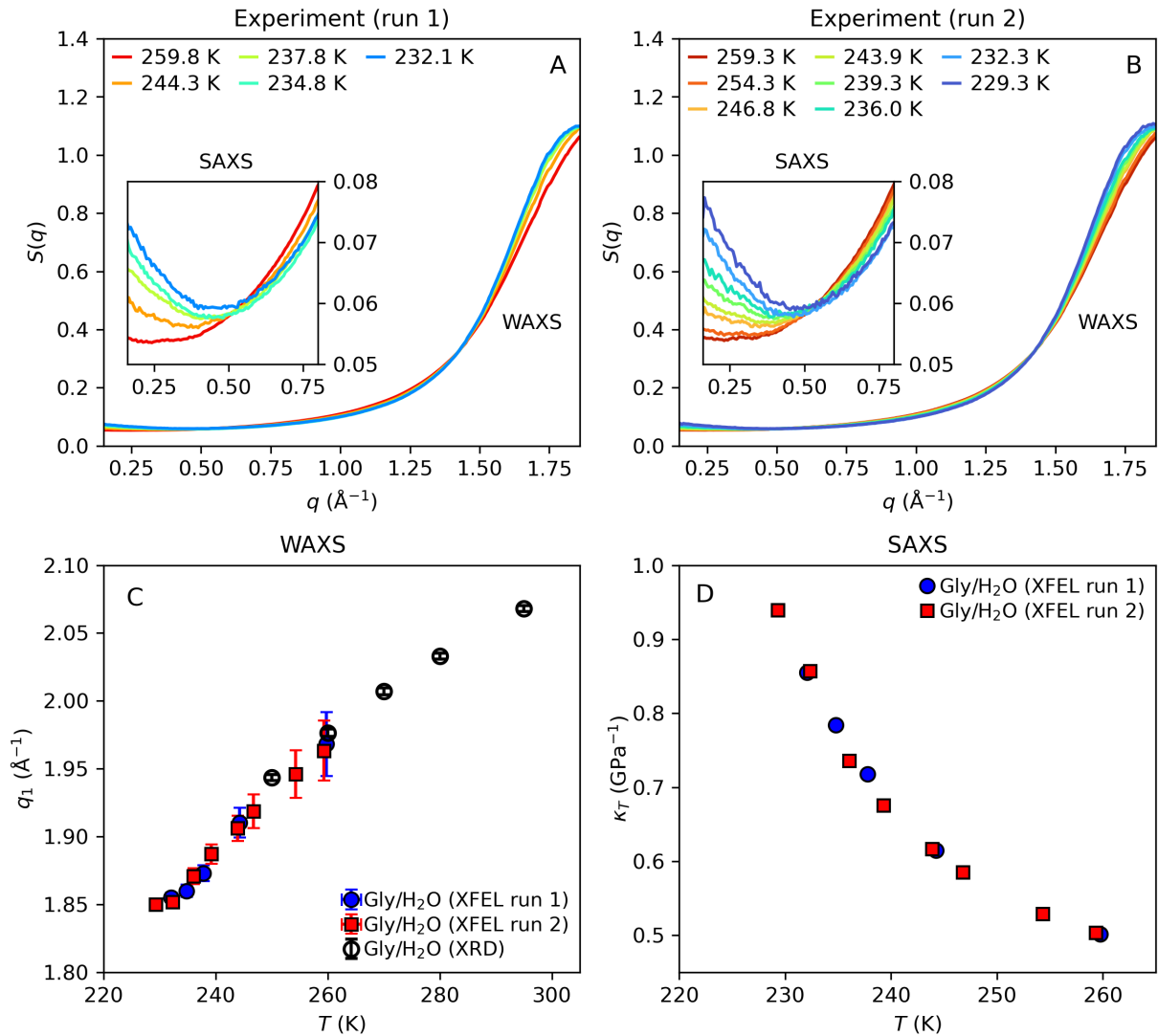
$$S(q) \simeq 1 + 4\pi\bar{\rho} \int_0^\infty r[g(r) - 1]\frac{\sin(qr)}{q} \ dr \ . \tag{S13}$$

Supplementary Figure. 3 | Molecular dynamics (MD) simulations of glycerol-water solution ($\chi_g = 3.2\%$ glycerol mole fraction) at different temperatures. (A) The radial distribution function $g(r)$ versus the radial distance r. The $g(r)$ is calculated by considering all the heavy atoms (O and C) in the solution and excluding the H atoms. (B) The structure factor $S(q)$ calculated from the $g(r)$ shown in panel (A), according to Eq. S13.

Supplementary Note 1.4 Reproducibility and control of experimental conditions

The reproducibility of the measurements can be confirmed by the data obtained during two independent runs, illustrated in Fig. S4. During run 1, we were able to reach temperatures from 259.8 K down to 232.1K, whereas in run 2 we could access the range from 259.3 K down to 229.3 K. We observe that the data is highly reproducible within the experimental error bars as can be seen by the comparison in the $S(q)$ line shape (Fig. S4A and B), but also from the temperature dependence of the q_1 peak position and isothermal compressibility κ_T (Fig. S4C and D). As an additional independent experimental control, we have also included data collected with a tabletop X-ray diffractometer (empty circles in Fig. S4C), which aligns well with the XFEL data. This consistency among various independent measurements validates our results and indicates that the observed trends are independent of changes in the experimental configuration.
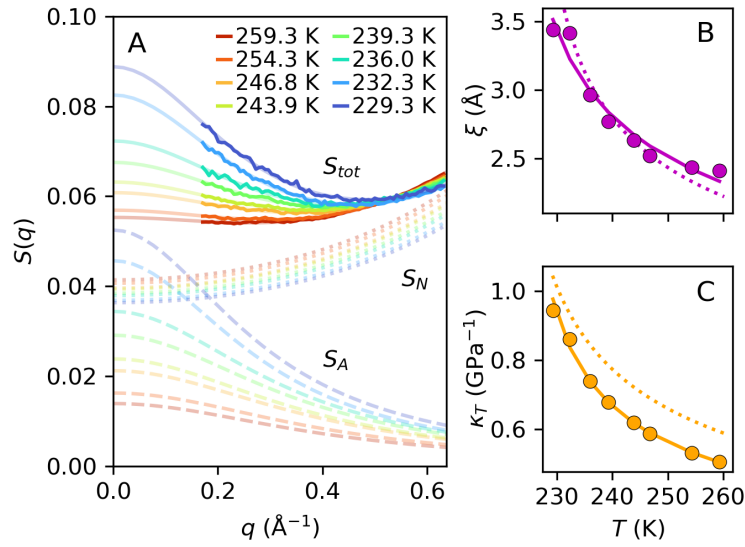

Supplementary Figure. 4 | Reproducibility and control of experimental results. (A-B) The structure factor $S(q)$ obtained during two independent measurements (run 1 and run 2). (C-D) The corresponding $S(q)$ peak position, q_1, and isothermal compressibility, κ_T obtained for the two runs. Errorbars indicate the standard error.

Supplementary Note 2   Experimental small-angle X-ray scattering analysis

The small-angle X-ray scattering structure factor is presented in Supplementary Figure 5A. The structure factor was obtained from the glycerol-water microdroplets ($\chi_g = 3.2\%$ glycerol mole fraction) at SACLA XFEL. The structure factor S_{tot} is decomposed as

$$S_{tot}(q) = S_N(q) + S_A(q) \tag{S14}$$

where S_N and S_A are the normal and anomalous components, respectively, of the structure factor (see main manuscript).

Supplementary Figure. 5 | Analysis of the small-angle X-ray scattering (SAXS) of glycerol-water microdroplets ($\chi_g = 3.2\%$ glycerol mole fraction) obtained at SACLA XFEL. (A) Decomposition of the total SAXS structure factor (S_{tot}) into normal (S_N, dotted lines) and anomalous (S_A, dashed lines) components. The experimental data for different temperatures is shown as full-colored solid lines while shaded solid lines denote the fits according to Eq.S14 (see also Methods in the main manuscript). Sub-panels (B) and (C) show the correlation length ξ and isothermal compressibility κ_T extracted from the fits in A. The lines are power law fits to the correlation length and isothermal compressibility according to Eq. (2) in the main manuscript for glycerol-water solution (solid lines) and pure water (dashed lines) from Ref. [8].

Supplementary Note 3 Droplet temperature estimation

The Knudsen evaporation model employed in this work for the estimation of the droplet temperature has been validated in prior studies, including both experimental approaches [6, 9], as well as molecular dynamics (MD) simulations [10]. Given the small deviation observed within independent datasets, we conclude that the temperature of the microdroplet for a given travel time is relatively homogeneous, in agreement with previous studies [6, 9].

We account for the glycerol-water mixture ($\chi_g = 3.2\%$ glycerol mole fraction) by including interpolated experimental thermodynamic parameters of the mixture in the evaporation model. In the Knuden evaporation theory, the evaporation rate Γ, i.e. the rate at which molecules evaporate from the droplet surface, after travel time t is given by

$$\Gamma(t) = \gamma \frac{P^*_{vap}(T_s) A_s(t)}{\sqrt{2\pi m k_B T_s}}. \tag{S15}$$

Here, $P^*_{vap} = P_{vap} - P_0$ is the effective saturation vapor pressure where P_{vap} is the saturation pressure of the mixture and P_0 is the chamber vacuum pressure. $T_s = T_s(t)$ is the current temperature in the droplet surface layer, A_s is the droplet surface area, m is the average molecular mass, and k_B is the Boltzmann constant. Due to the low glycerol concentration, we approximate the evaporation coefficient with $\gamma = 1$ used previously for pure water [10]. The cooling rate on the droplet surface due to evaporation is

$$\frac{dT_s}{dt} = -\Gamma(t) \left[\frac{\Delta H_{vap}(T_s)}{C_p(T_s)\Delta V_s(t)\rho(T_s)} \right], \tag{S16}$$

where ΔH_{vap} is the evaporation enthalpy, C_p is the isobaric heat capacity and ρ is the density of the mixture. V_s is the volume of the droplet surface layer.

As previously done in Refs. [6, 9, 10], the droplet is divided into n spherical shells and the temperature of the droplet is calculated numerically by estimating the heat conduction between shells as a function of time. The heat flow, dQ/dt, between shell n and $n + 1$ is calculated using the Fourier's law of thermal conduction

$$\frac{dQ}{dt} = -\frac{4\pi r_n^2 \kappa(T_n)}{\Delta r(t)} [T_{n+1} - T_n], \tag{S17}$$

where κ is the thermal conductivity of the mixture, Δr is the shell thickness; r_n and T_n are the outer radius and the current temperature of shell n, respectively. The temperature change due to heat flow between shells is then given by

$$dT_n = \frac{\Delta Q}{C_p(T_n) M_n}, \tag{S18}$$

where ΔQ is the net heat flowing into shell n, $M_n = \Delta V_n \rho(T_n)$ is the shell mass and ΔV_n is the shell volume.

Due to the large mass difference and the low vapor pressure of glycerol compared to water, we assume that only water molecules evaporate. During the numerical calculation [6, 9, 10], the droplet radius r is updated after each iteration (i.e, time step dt) by accounting for the droplet volume change due to the number of evaporated water molecules n_{evap}:

$$\frac{r^3(t)}{r_0^3} = \frac{V(t)}{V_0} = \frac{V_0 - n_{evap}(t)V_m}{V_0} \tag{S19}$$

where $n_{evap}(t) = \Gamma(t)dt$ and V is the droplet volume. V_m is the molar volume of water in the mixture, which is approximated by the molar volume in pure water. In addition, after each iteration, we account for the slightly increased glycerol molar fraction x_g

$$x_g(t) = \frac{n_g}{n_g + (n_w - n_{evap}(t))}, \tag{S20}$$

where n_g and n_w are the initial number of molecules of glycerol and water, respectively.

The average droplet temperature $T(t)$ is calculated by averaging the temperatures $\{T_n\}$ of the shells. The resulting estimated droplet temperatures and glycerol concentrations are presented in Supplementary Figure 7F. The droplet travel time t in the vacuum chamber is calculated from the known travelled droplet distance z from the liquid jet nozzle, the droplet frequency f and the droplet-droplet distance l_{dd}, as
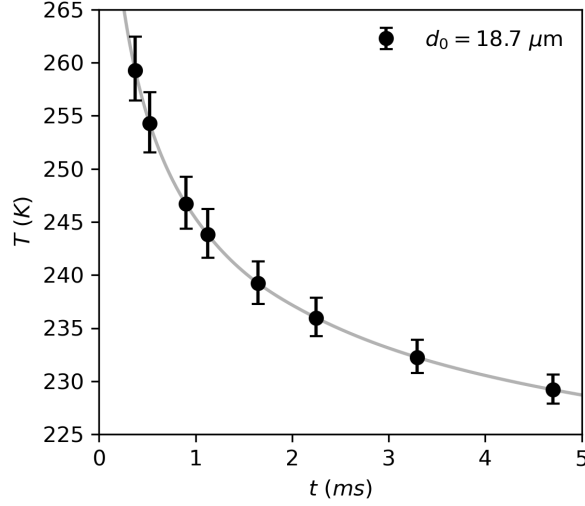
$$t = \frac{z}{f \cdot l_{dd}}. \tag{S21}$$

Both the initial droplet radius r_0 and the droplet-droplet distance l_{dd} are calibrated from *in situ* optical microscope images. The thermodynamic properties and the input parameters used for the temperature estimation are summarized in Supplementary Figure 7A-E and Table 1, respectively.

We estimate that the main source of experimental uncertainty in the droplet temperature estimation by Knudsen theory is likely the droplet size. This uncertainty arises from the size determination from 2D microscope images, where the cross-section of the 3D droplets depends on the camera sharpness and focusing. Based on the microscope images, we estimate that the uncertainty in the droplet diameter is, at most, $\sigma_d=\pm 3$ μm, where d_0=18.7 μm is the determined droplet diameter. Such deviations in droplet size would result in different droplet temperatures calculated with Knudsen evaporation theory.

The resulting uncertainty in the temperature decreases upon cooling, from approximately $\approx$3 K at $T_0 = 260$ K to $\approx$1 K at $T_0 = 230$ K (Fig. S6). Therefore, we conclude that the uncertainty in droplet size and temperature should not significantly alter the observed temperature trends of the experimental q_1 position and compressibility κ_T. Furthermore, the high level of data reproducibility suggests that the underlying physical processes influencing the droplet behavior remain robust despite any minor variations in droplet temperature.

Supplementary Table 1 | Droplet temperature estimation parameters

Glycerol molar (mass) fraction	x_g (w_g)	3.2% (14.5 wt%)
Droplet diameter	$2r_0$	18.7 μm
Droplet-droplet distance	l_{dd}	85.5 μm
Droplet frequency	f	157 kHz
Travel distances	z	5−65 mm
Initial temperature	T_0	298 K
Chamber vacuum pressure	P_0	1.60 Pa
Time step	dt	1 ns and 10 ns
Number of time steps	N_{steps}	700 000
Number of spherical shells	N_{shells}	100
Evaporation coefficient	γ	1

Supplementary Figure. 6 | Droplet temperature estimation calculated with Knudsen evaporation theory for droplets with size $d_0 = 18.7\ \mu m$. The errorbars convey the temperature uncertainty upon cooling, for a droplet size of $\sigma_d = \pm 3\ \mu m$.

Supplementary Note 3.1 Thermodynamic properties of glycerol-water mixtures

Supplementary Note 3.1.1 Density

The density ρ of the glycerol-water mixture is estimated using an empirical formula from Ref. [11]:

$$\rho(T, w_g > 0) = 1 + A(T) \sin(w_g^{1.31}\pi)^{0.81} \left[\rho_w(T) + \frac{\rho_g(T) - \rho_w(T)}{1 + \frac{\rho_g(T)}{\rho_w(T)}\left(\frac{1}{w_g} - 1\right)} \right], \tag{S22}$$

where $A(T) = 1.78 \cdot 10^{-6}T^2 - 1.82 \cdot 10^{-4}T + 1.41 \cdot 10^{-2}$, ρ_w is the density of pure water, ρ_g is the density of pure glycerol, w_g is the mass fraction of glycerol. For the density of liquid glycerol we interpolate experimental density data between 156–311 K from Ref. [12], while for water we use an interpolation of experimental density data of hexagonal ice and liquid water from Ref. [13], as used previously [9].

Supplementary Note 3.1.2 Saturation vapor pressure

To estimate the saturation vapor pressure P_{vap} of the glycerol-water mixture utilize an interpolation of experimental data of the concentration-dependent relative vapor pressure P_{rel} of the mixture compared to pure water (at $T = 273.15$ K) from Ref. [14]. Thus,
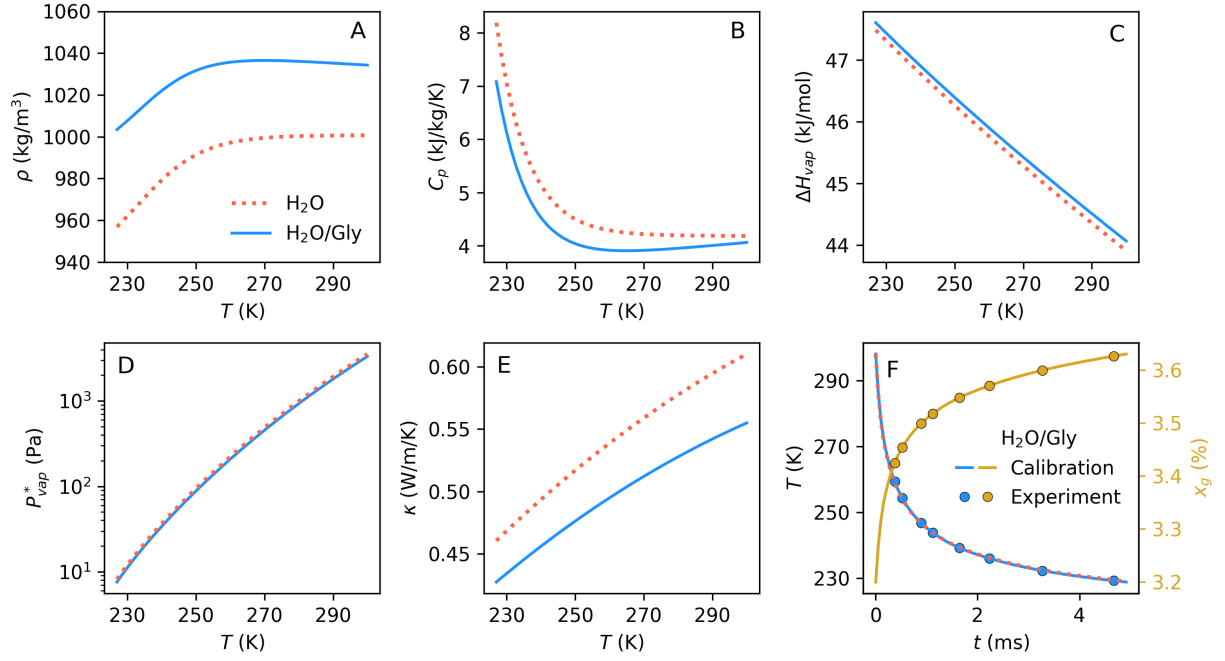
$$P_{vap}(T, x_g) = P_{vap,w}(T) \cdot P_{rel}(x_g), \tag{S23}$$

where $P_{vap,w}$ is the saturation vapor pressure of water from Ref. [15], as used previously [9].

Supplementary Note 3.1.3 Isobaric heat capacity

For the isobaric heat capacity C_p we use a mass-fraction weighted formula as suggested in Ref. [16],

$$C_p(T, w_g) = \frac{(1 - w_g)C_{p,w}(T)}{1 + aw_g^b} + w_g \left[cB(T) + d \right], \tag{S24}$$

Supplementary Figure. 7 | (A-E) Thermodynamic properties of glycerol-water solution ($\chi_g = 3.2\%$ glycerol mole fraction, blue), compared that of pure water (red), used for the droplet temperature calculations; density ρ, isobaric heat capacity C_p, vaporization enthalpy ΔH_{vap} and effective vapor pressure P_{vap}^* for vacuum chamber pressure $P_0 = 1.6$ Pa, and thermal conductivity κ. (F) The estimated droplet temperature as a function of travel time from the liquid jet nozzle, where curves for pure water and the mixture are nearly overlapping. The slightly increasing glycerol molar fraction x_g versus travel time for the mixture is shown in yellow (right axis).

where $B(T)$ is a baseline (first degree polynomial) determined from a fit to experimental C_p data of 65 wt% glycerol-water mixture, while a, b, c and d are constants obtained by fitting the entire Eq. S24 to experimental data in the range 25–65 wt% glycerol-water from Ref. [14]. As previously [9], for the isobaric heat capacity of pure water $C_{p,w}$ we use an interpolation of experimental data from Ref. [17].

Supplementary Note 3.1.4 Enthalpy of vaporization

To estimate the enthalpy of vaporization H_{vap} for the glycerol-water solution we use a theoretical formula for binary mixtures derived in Ref. [18]:

$$\Delta H_{vap}(T, x_g) = -RT \ln \left[\frac{P_{vap}(T, x_g)}{P_{vap,w}(T)} \right] + \Delta H_{vap,w}(T), \tag{S25}$$

where R is the ideal gas constant and $H_{vap,w}$ is the vaporization enthalpy for pure water from Ref. [19], as used previously [9].
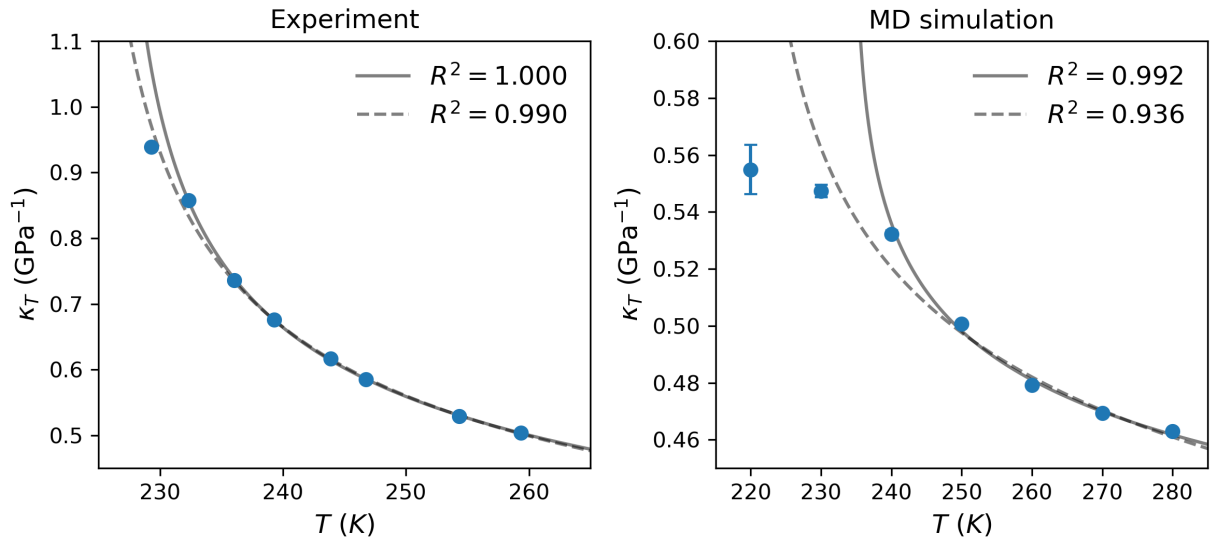
Supplementary Note 3.1.5 Thermal conductivity

The thermal conductivity of the glycerol-water mixture is calculated as a mass-fraction weighted average of the thermal conductivity for pure water κ_w, as previously by interpolating experimental data from Ref. [20], and the linearly temperature-dependent thermal conductivity for pure glycerol κ_g from Ref. [14]:

$$\kappa(T, w_g) = (1 - w_g)\kappa_w(T) + w_g\kappa_g(T) \tag{S26}$$

The accuracy of the above formula was checked against experimental data for glycerol-water mixtures from Ref. [14] providing good agreement for concentrations ranging up to 50 wt% glycerol.

Supplementary Note 4 Compressibility Power law R^2 analysis

Supplementary Figure. 8 | Comparison of the isothermal compressibility κ_T(T) of glycerol-water obtained from (A) the experiment and (B) the MD simulations. The lines depict power-law fits for different temperature ranges, with (dashed line) and without (solid line) the κ_T at $T = 230K$. Based on the goodness of the fit (R^2 shown in the legend) we observe that both experimental and MD data indicate deviation from the power law behavior at $T = 230K$. Errorbars indicate the standard error.

Supplementary Note 5 MD Simulations Additional Information and Comparisons

The CHARMM36 force field [21, 22] was used to represent the glycerol molecules and the TIP4P/2005 model was used to model the water molecules [23]. The CHARMM force field is a well-known additive, all-atom force field that has been used extensively in the past to study proteins, nucleic acids, lipids, and carbohydrates. The CHARMM force field combined with the TIP4P/2005 water model have been used in the past to study the structural, dynamical, and thermodynamic properties of glycerol-water [24–29]. Our rationale for employing the TIP4P/2005 water model is that it reproduces very well the properties of bulk water and many of the properties of glycerol-water mixtures [26–28]. In particular, the TIP4P/2005 water model reproduces qualitatively well the anomalous properties of water, including the compressibility maximum at 1 bar, and it exhibits a liquid-liquid critical point [30].
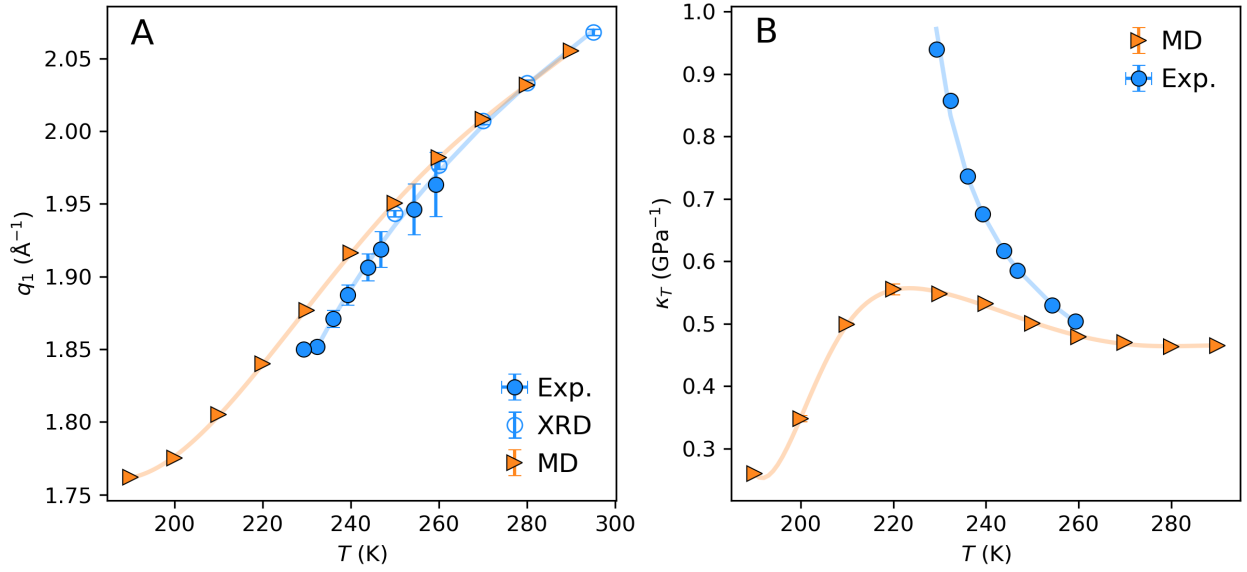
Supplementary Note 5.1 Comparison of experimental and MD results

We note that our results from MD simulations, based on the CHARMM36 force field and TIP4P/2005 water model, are in very good agreement with the experiments. To show this we consider a glycerol-water solution with $\chi_g = 3.2\%$ glycerol mole fraction and compare the location of the first peak of the structure factor, q_1, obtained from experiments and MD simulations. As shown in Fig. S9A, the values of q_1 obtained from experiments and MD simulations are in very good agreement with each other, particularly at T>255 K. At lower temperatures, the values of q_1 obtained from MD simulations appear to deviate slightly from the experimental values. A similar trend is observed in the values of q_1 reported from MD simulations of bulk water [30]. Since the q_1 position correlates with the tetrahedrality fraction of water [6], this observation indicates that TIP4P/2005 can underestimate the tetrahedral local coordination at ambient pressure.
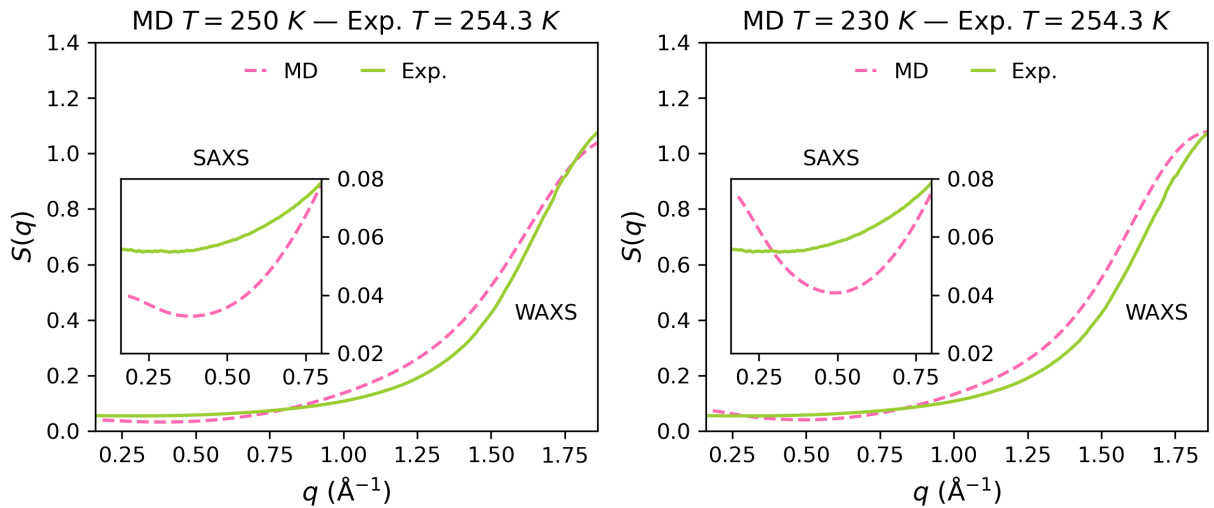
The isothermal compressibility κ_T of the glycerol-water solution ($\chi_g = 3.2\%$) calculated from (i) the experimental structure factor measured in the XFEL experiment and (ii) the MD simulations are included in Fig. S9B. As for the case of pure TIP4P/2005 water, the MD simulations of the glycerol-water mixture reproduce the qualitative increase of κ_T upon cooling. However, our MD simulations underestimate the value of κ_T relative to the experiments. This is not surprising since most empirical rigid/flexible water models, including the TIP4P/2005 model, underestimate the values of κ_T of bulk water at low temperatures [30]. Despite this limitation inherent to most of the available water models, our results from MD simulations in Fig. S9B clearly show a maximum in the κ_T of the glycerol-water solution ($\chi_g = 3.2\%$) at $T \approx 223\ K$, at temperatures slightly below the lowest temperature accessed in our experiments.

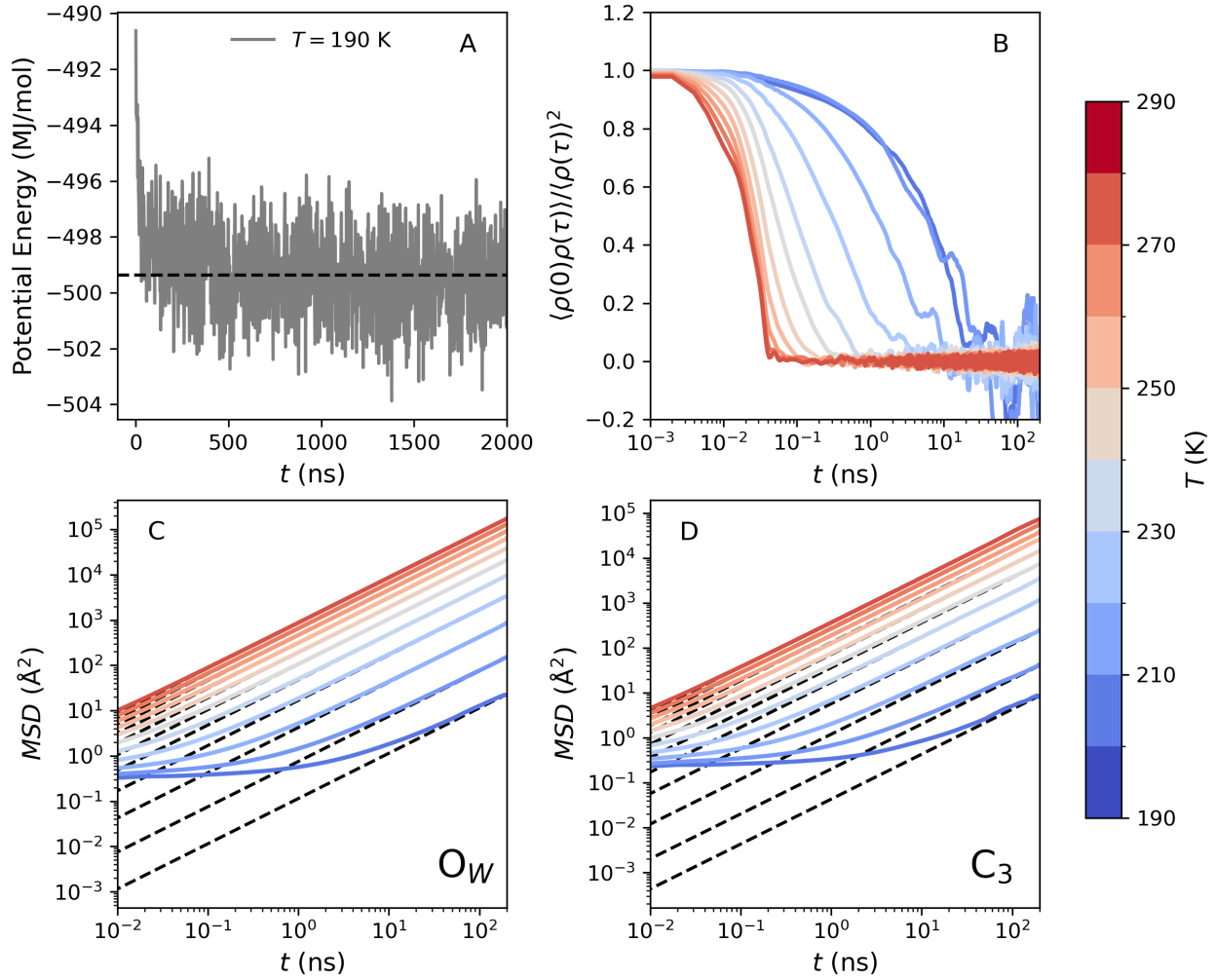## Supplementary Note 5.2 Equilibration check and Production run details

The equilibration time ranged from 200 ns at $T = 290$ K to 2 µs at 190 K based on time-dependence of the potential energy shown in Fig. S11. The corresponding simulation time for the production runs was 200 ns and was determined based on the characteristic correlation time obtained from the density-density correlation functions, as shown in Fig. S11. This approach ensures full decorrelation within the production run and allows complete sampling of the density fluctuations at lower temperatures. In addition, we confirm that the mean-square displacement of glycerol and water becomes a linear function of time within the simulation time for the production runs, i.e., both the glycerol and water molecules reach the diffusive regime (see Fig. S11C and Fig. S11D).

Supplementary Figure. 9 | (A) Comparison of the structure factor first-peak position, $q_1(T)$, obtained from XFEL and XRD experiments (blue filled and empty circles respectively), as well as those from MD simulations (orange triangles) of the studied glycerol-water solution ($\chi_g = 3.2\%$ glycerol mole fraction). The agreement between experiments and MD simulations at $T > 229$ K is remarkably good. (B) Temperature dependence of the isothermal compressibility κ_T of the glycerol-water solution calculated from the experimental structure factor from the XFEL experiment (blue circles) and the MD simulations (orange triangles). As for the case of pure TIP4P/2005 water, the MD simulations of the glycerol-water mixture reproduce the qualitative increase of κ_T upon cooling although they underestimate the value of κ_T relative to the experiments. Note that MD simulations show a clear maxima in the κ_T of the solution at $T \approx 230$ K. Errorbars indicate the standard error.
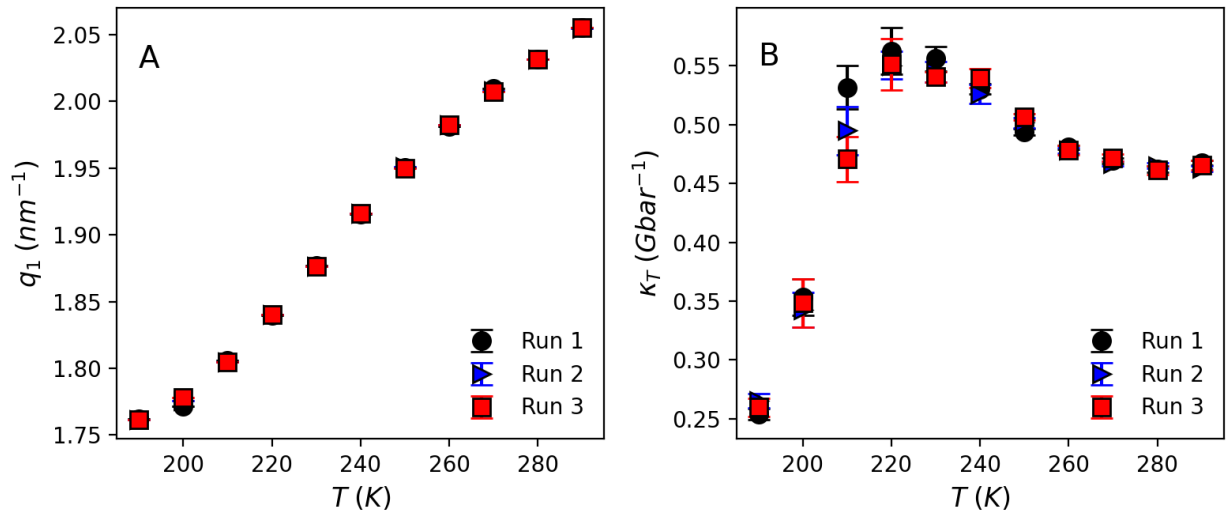

Supplementary Figure. 10 | Direct comparison of the structure factor $S(q)$ obtained from experiment (solid line) and MD simulations (dashed line) for (a) similar temperatures near $T = 250\ K$ and (b) similar supercooling degrees taking into account the melting point for TIP4P/2005 ($T_m \approx 250\ K$ at $P = 1$bar).
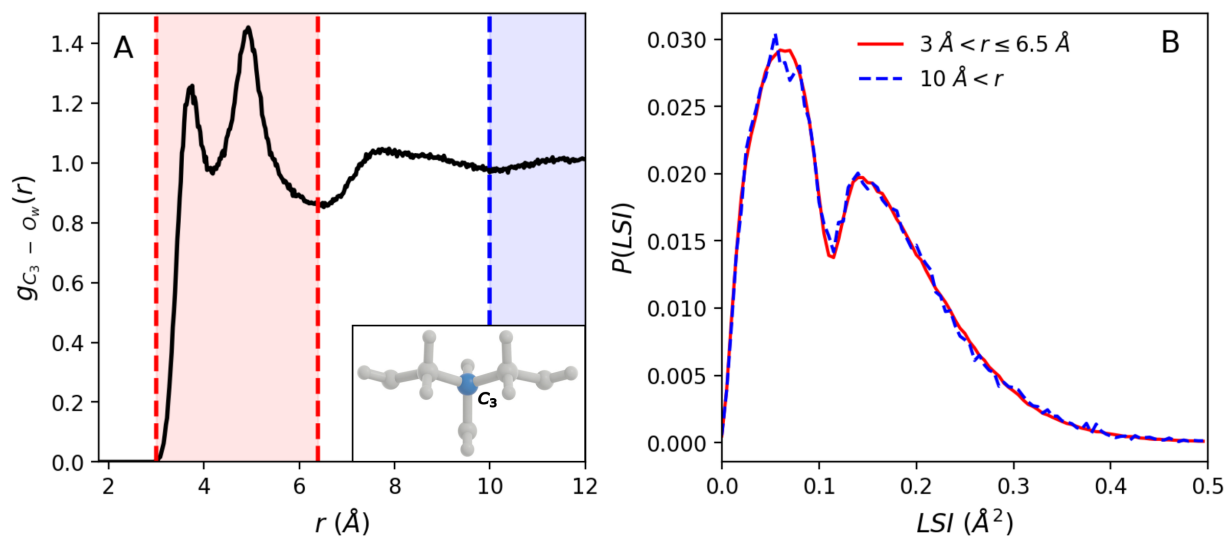
Supplementary Figure. 11 | (A) Potential energy as a function of time during the equilibration of all MD simulations of the glycerol-water solution at T=190K. The horizontal black dashed line represents the average of the last 100 data points and serves as a visual guide. (B) Density-density time correlation of the MD simulations (production runs) of water-glycerol for different temperatures shown in the legend. We observe that full decorrelation occurs within 200 ns, which is the simulation time of the production runs for each temperature. (C) The mean-square displacement of water (with reference to the oxygen, O_W) and (D) that of glycerol (with reference to the central carbon, C_3).

Supplementary Note 5.3 Reproducibility of MD simulations

Supplementary Figure. 12 | Results from three MD simulations of a glycerol-water solution at $P = 1$bar ($\chi_g = 3.2\%$); MD simulations start from a different starting configuration. (A) Position of the structure factor first peak, $q_1(T)$, and (B) isothermal compressibility, $\kappa_T(T)$, as a function of temperature. The values of $q_1(T)$ and $\kappa_T(T)$ are reproducible among the three runs within the error bars. The MD simulation results reported in the main manuscript are the average values of the three runs shown here. Errorbars indicate the standard error.

Supplementary Note 6 Analysis of solvation layer composition from MD simulations

Supplementary Figure. 13 | (A) Site-site partial radial distribution function (RDF) between the central carbon of glycerol (C_3) and the oxygen atoms of water (O_W). The regions corresponding to the first and second hydration shell (3Å$< r <$ 6.5Å) and the bulk region ($r >$ 10Å) are shaded in red and blue, respectively. A representation of a glycerol molecule is included in the inset, with the central carbon highlighted. (B) Comparison of the inherent Local Structure Index (LSI) for water in the first/second hydration shell (solid red line) and in the bulk region (dashed blue line).

References

1. Als-Nielsen, J. & McMorrow, D. in *Elements of Modern X-ray Physics* 1st ed., 113–146 (Chichester, West Sussex, United Kingdom, 2011).

2. Krogh-Moe, J. A method for converting experimental X-ray intensities to an absolute scale. *Acta Cryst.* **9,** 951–953 (1956).

3. Norman, N. The Fourier transform method for normalizing intensities. *Acta Cryst.* **10,** 370–373 (1957).

4. Biehl, R. Jscatter, a program for evaluation and analysis of experimental data. *PLoS One* **14,** e0218789 (2019).

5. Wang, J., Tripathi, A. N. & Smith, V. H. Chemical binding and electron correlation effects in x-ray and high energy electron scattering. *J. Chem. Phys.* **101,** 4842–4854 (1994).

6. Kim, K. H. *et al.* Maxima in the thermodynamic response and correlation functions of deeply super-cooled water. *Science* **358,** 1589 (2017).

7. Hubbell, J. H. *et al.* Atomic form factors, incoherent scattering functions, and photon scattering cross sections. *J. Phys. Chem. Ref. Data* **4,** 471–538 (1975).

8. Späh, A. *et al.* Apparent power-law behavior of water's isothermal compressibility and correlation length upon supercooling. *Phys. Chem. Chem. Phys.* **21,** 26–31 (2018).

9. Sellberg, J. A. *et al.* Ultrafast X-ray probing of water structure below the homogeneous ice nucleation temperature. *Nature* **510,** 381 (2014).

10. Schlesinger, D., Sellberg, J. A., Nilsson, A. & Pettersson, L. G. M. Evaporative cooling of microscopic water droplets in vacuo: Molecular dynamics simulations and kinetic gas theory. *J. Chem. Phys.* **144,** 124502 (2016).

11. Volk, A. & Kähler, C. J. Density model for aqueous glycerol solutions. *Exp. Fluids* **59,** 75 (2018).

12. Blazhnov, I. V., Malomuzh, N. P. & Lishchuk, S. V. Temperature dependence of density, thermal expansion coefficient and shear viscosity of supercooled glycerol as a reflection of its structure. *J. Chem. Phys.* **121,** 6435–6441 (2004).

13. Kell, G. S. Density, thermal expansivity, and compressibility of liquid water from 0.deg. to 150.deg.. Correlations and tables for atmospheric pressure and saturation reviewed and expressed on 1968 temperature scale. *J. Chem. Eng. Data* **20,** 97–105 (1975).

14. Soap and Detergent Association. *Physical Properties of Glycerine and its Solutions* (New York, 1963).

15. Murphy, D. M. & Koop, T. Review of the vapour pressures of ice and supercooled water for atmospheric applications. *Q. J. Roy. Meteorol. Soc.* **131,** 1539–1565 (2005).

16. Biddle, J. W., Holten, V. & Anisimov, M. A. Behavior of supercooled aqueous solutions stemming from hidden liquid–liquid transition in water. *J. Chem. Phys.* **141,** 074504 (2014).

17. Angell, C. A., Sichina, W. J. & Oguni, M. Heat capacity of water at extremes of supercooling and superheating. *J. Phys. Chem.* **86,** 998–1002 (1982).

18. Dobruskin, V. K. *Effect of Chemical Composition on Enthalpy of Evaporation and Equilibrium Vapor Pressure* 2010.

19. Somayajulu, G. R. New equations for enthalpy of vaporization from the triple point to the critical point. *Int. J. Thermophys.* **9,** 567–575 (1988).

20. Lide, D. R. *CRC Handbook of Chemistry and Physics* 90th ed. (Boca Raton, 2010).

21. Vanommeslaeghe, K. *et al.* CHARMM general force field: A force field for drug-like molecules compatible with the CHARMM all-atom additive biological force fields. *J. Comput. Chem.* **31,** 671–690 (2010).

22. Reiling, S., Schlenkrich, M. & Brickmann, J. Force field parameters for carbohydrates. *J. Comput. Chem.* **17,** 450–468 (1996).

23. Abascal, J. L. F. & Vega, C. A general purpose model for the condensed phases of water: TIP4P/2005. *J. Chem. Phys.* **123,** 234505 (2005).

24. Egorov, A. V., Lyubartsev, A. P. & Laaksonen, A. Molecular Dynamics Simulation Study of Glycerol–Water Liquid Mixtures. *J. Phys. Chem. B* **115,** 14572–14581 (2011).

25. Dashnau, J. L., Nucci, N. V., Sharp, K. A. & Vanderkooi, J. M. Hydrogen Bonding and the Cryoprotective Properties of Glycerol/Water Mixtures. *J. Phys. Chem. B* **110,** 13670–13677 (2006).

26. Jahn, D. A., Wong, J., Bachler, J., Loerting, T. & Giovambattista, N. Glass polymorphism in glycerol–water mixtures: I. A computer simulation study. *Phys. Chem. Chem. Phys.* **18,** 11042–11057 (2016).

27. Jahn, D. A., Akinkunmi, F. O. & Giovambattista, N. Effects of Temperature on the Properties of Glycerol: A Computer Simulation Study of Five Different Force Fields. *J. Phys. Chem. B* **118,** 11284–11294 (2014).

28. Akinkunmi, F. O., Jahn, D. A. & Giovambattista, N. Effects of Temperature on the Thermodynamic and Dynamical Properties of Glycerol–Water Mixtures: A Computer Simulation Study of Three Different Force Fields. *J. Phys. Chem. B* **119,** 6250–6261 (2015).

29. Daschakraborty, S. How do glycerol and dimethyl sulphoxide affect local tetrahedral structure of water around a nonpolar solute at low temperature? Importance of preferential interaction. *J. Chem. Phys.* **148,** 134501 (2018).

30. Pathak, H. *et al.* Temperature dependent anomalous fluctuations in water: shift of $\approx$1 kbar between experiment and classical force field simulations. *Mol. Phys.* **117** (2019).